scientific reports

OPEN

Numerical study on fatigue failure mechanism of reinforced concrete slabs under coupled action of corrosion and cyclic loading

Shuyong Wang[1,2]✉, Qiu Zhao[1]✉, Pengcheng Song[3] & Fei Yang[4]

Based on three-dimensional scanning technology, a database of real block stone shapes with varying particle sizes was established, and discrete element models of reinforced concrete with different corrosion rates were developed, accounting for the particle crushing effect. Four-point bending fatigue numerical simulations were conducted on reinforced concrete models with corrosion rates of 0%, 10%, 25%, and 40% to investigate their mechanical characteristics, failure modes, damage evolution, force chain distribution, and energy dissipation. The aim was to reveal the influence mechanism of corrosion on the fatigue performance of reinforced concrete.The results show that for uncorroded specimens, the stiffness ratio decreases gradually, with a residual stiffness of 60%. At a corrosion rate of 40%, the stiffness ratio exhibits a cliff-like drop, leaving only 30% residual stiffness. Deflection growth is markedly accelerated, and the deformation capacity of the structure deteriorates significantly. In terms of failure mode, corrosion causes a gradual transition from ductile bending failure to brittle shear failure. This shift indicates a substantial reduction in both load-bearing capacity and structural safety margin. Damage process analysis reveals that acoustic emission intensity progresses through three stages: micro-crack initiation, stable crack propagation, and rapid crack expansion leading to structural instability. Corrosion accelerates both the initiation and propagation of micro-cracks, causing rapid accumulation and coalescence of internal damage. This process is accompanied by the absorption and release of strain energy, with the peak strain energy of highly corroded specimens decreasing by more than 80%. Regarding force chain distribution, uncorroded specimens have 25% of their force-chains classified as strong, forming an optimal load-transfer path oriented at approximately 45°. As the corrosion rate increases, the proportion of strong force-chains gradually declines.

Keywords Reinforced concrete slab, Three-dimensional scanning, Fatigue load, Corrosion effect, Macroscopic mechanical, Micro-mechanism

Bridges serve as critical "throats" of highway transportation networks and play a pivotal role in national transportation systems[1]. Owing to their simple structure, ease of fabrication, and cost-effectiveness, reinforced concrete (RC) is extensively used in highway bridge construction. In recent years, rapid economic growth has led to increased traffic volumes on existing bridges worldwide, often accompanied by frequent overloading and other adverse factors. These conditions have significantly accelerated the accumulation of fatigue damage, making fatigue failure one of the primary causes of bridge accidents. For RC bridges, fatigue failure is typically driven by fatigue damage to the bridge deck[2], yet fatigue considerations are often neglected in deck design. Research on the fatigue behavior of RC slabs remains limited, and their failure mechanisms are still not fully understood. Consequently, it is of considerable importance to investigate the interaction between steel reinforcement and concrete from both macro- and micro-scale perspectives, and to analyze the evolution of structural fracture and damage mechanisms. Such studies will help advance the theoretical framework for fatigue failure in RC slabs and ensure the safe, long-term operation of highway bridges under cyclic loading.

Currently, most experimental studies on RC bridge deck fatigue rely on laboratory testing methods. For example, Wang et al.[3] investigated the static and fatigue bending behavior of ultra-high-performance fiber-

[1]College of Civil Engineering, Fuzhou University, Fuzhou 350116, Fujian, China. [2]School of Civil Engineering and Architecture, Taizhou University, Taizhou 318000, Zhejiang, China. [3]Agriculture and Rural Bureau of Chuanying District, Jilin 132011, Jilin, China. [4]Zhejiang Yubo New Material Co., Ltd, Taizhou 318000, Zhejiang, China. ✉email: wangshuyong163@163.com; zhaoqiu@fzu.edu.cn

reinforced concrete (UHPFRC) bridge decks through four-point bending tests. Their results indicated that UHPFRC decks enhance structural stiffness and crack resistance, reduce mid-span deflection and crack propagation rates, significantly lower deck weight, and improve fatigue life. Liu and Yang[4] examined the effects of bolt and apertured steel plate arrangement, shear span ratio, and fatigue load amplitude on the damage evolution and failure mode of steel-plate-concrete composite slabs using static and constant-amplitude fatigue tests. They found that fatigue stress amplitude has a direct influence on fatigue life, whereas bolt arrangement and the number of apertured steel plates have minimal effect. Failure was ultimately governed by fatigue fracture of the bottom steel plate, followed by crushing of the compression-zone concrete. Based on these findings, Liu and Yang proposed a method to predict stiffness evolution and fatigue life for such composite slabs. Mai et al.[5] performed four-point bending tests to study the fatigue behavior of basalt fiber-reinforced polymer (BFRP) bar-reinforced sea-sand concrete (SSC) slabs, focusing on stress level, crack propagation, deflection, and stiffness. They reported that fatigue failure was primarily caused by fracture of the BFRP reinforcement, and that specimens subjected to fatigue exhibited more cracks than those failing under static loading. Additionally, the load-deflection curve during the first cycle displayed a bilinear form with the cracking load as the inflection point, while in subsequent cycles it became linear. Yan et al.[6] investigated the internal fatigue damage evolution of continuous steel-concrete composite (CSCC) beams using acoustic emission (AE) monitoring. They developed a fatigue life prediction model based on cumulative AE energy, finding that AE techniques provide effective real-time monitoring of fatigue damage in composite materials. The fatigue damage-energy relationship of CSCC beams followed an exponential function, which can reliably predict both the damage progression and fatigue life of such structures.

In summary, laboratory tests can directly capture changes in the macroscopic mechanical properties of RC specimens under actual fatigue loading. Such tests provide accurate and reliable results, offering a solid data foundation for theoretical studies. However, they also have notable limitations: long testing cycles, high labor and time requirements for complex or large-scale fatigue loading, substantial costs, significant investment in equipment and personnel, and difficulty in fully replicating the complex loading and environmental conditions of real-world structures. Moreover, conventional tests have limited capability to observe microscopic damage, making it challenging to accurately detect micro-cracks in concrete or subtle changes in the bond properties between steel reinforcement and concrete. Numerical simulation technology can effectively overcome these shortcomings. It enables rapid, large-scale computation and flexible modeling of fatigue failure processes under complex loading conditions at relatively low cost, while offering significant advantages in studying microscopic damage mechanisms. It also allows for in-depth analysis of the micro-scale processes involved in fatigue damage in composite materials. Therefore, for RC structures, fatigue damage mechanisms should be investigated more comprehensively, deeply, and efficiently through an integrated approach combining experimental research with numerical simulation.

With the rapid advancement of computer hardware and related scientific theories, numerical simulation techniques have been widely applied to the study of material mechanisms. Commonly used methods include the Finite Element Method (FEM)[7,8], Boundary Element Method (BEM)[9,10], Extended Finite Element Method (XFEM)[11,12], Meshless Methods[13], and Discrete Element Method (DEM)[14,15]. In FEM research, Zou et al.[7] used ABAQUS to investigate the effects of carbon fiber-reinforced polymer (CFRP) size, load level, and prestress level on the fatigue performance of side-bonded CFRP (SB-CFRP) strengthened RC. They developed a fatigue life prediction model for SB-CFRP-strengthened RC members. Al-Rousan et al.[8] performed three-dimensional nonlinear finite element analysis (NLFEA) to simulate the fatigue failure of RC bridge decks and examine the mechanical response of decks reinforced with CFRP and glass fiber-reinforced polymer (GFRP). Results showed that CFRP- and GFRP-reinforced decks outperformed conventional RC decks in ultimate load capacity, elastic stiffness, post-cracking stiffness, elastic energy absorption, and post-cracking energy absorption, while also reducing mid-span deflection.

In BEM studies, Uddin et al.[9] investigated the relationship between the stress intensity factor and crack growth increment in RC under three corrosion-induced cracking modes. They elucidated the crack propagation mechanism caused by steel reinforcement corrosion, confirming that the dominant cracking mode was Mode I. Ihsan et al.[10] improved RC corrosion assessment using BEM with field-measured data. By solving the Laplace equation via BEM, they determined the electric potential distribution in concrete structures. The results indicated that BEM improves the accuracy of corrosion assessment and field data interpretation, enabling more precise prediction of corrosion profiles in steel reinforcement.

In XFEM research, Faron and Rombach[11] conducted nonlinear numerical simulations of RC beams without transverse reinforcement, analyzing flexural and shear crack propagation without predefined notches. They compared load–deformation and crack width–load curves for different mesh densities, validating the simulated crack patterns against experimental results. Their findings accurately predicted fracture behavior, crack propagation, and internal force redistribution. El Yassari and El Ghoulbzouri[12] employed XFEM with a concrete damage plasticity model to simulate fiber-reinforced concrete (FRC) columns containing steel fibers, polypropylene fibers, and hybrid fiber mixes. They investigated crack initiation and propagation under quasi-static and cyclic loading, analyzed compressive and tensile performance using a reinforcement index (RI), and studied damage evolution under cyclic loading. The predicted hysteretic behavior matched well with previous experimental results.

In Meshless Methods, Yu et al.[13] proposed and validated an improved numerical approach for modeling freeze–thaw deterioration in pre-cracked concrete. Their simulations considered crack inclination, aggregate and pore content, and particle size. Findings showed that at low temperatures, pre-existing elliptical cracks generate “primary cracks” along the flaw direction and “secondary cracks” perpendicular to it; aggregates tend to “attract” frost cracks, while pores increase crack path curvature. This work aimed to elucidate the freeze–thaw damage mechanism in cracked concrete and provide theoretical and methodological support for cold-region structural design and Meshless Method optimization.

In DEM applications, Du[14] used Particle Flow Code (PFC) 2D to simulate flexural tests on RC beams, analyzing crack development and ultimate load capacity under varying notch positions and inclinations. Results showed that notches closer to mid-span or inclined nearer to 90° promoted longer and wider penetrating cracks. Changes in loading rate and particle arrangement also caused fluctuations in the load–deflection curve. Luo et al.[15] developed a DEM-based numerical model of cement-stabilized macadam, analyzing both its macroscopic mechanical properties and microscopic degradation under cyclic loading. They identified the evolution patterns of strain, cracking, contact damage ratio, and various energy components (strain, damping, frictional, bonding, and kinetic energy), thereby clarifying the fatigue failure mechanism. They also highlighted the significant influence of aggregate shape on simulation accuracy.

In summary, although the FEM is widely applied in simulating the mechanical behavior of complex structures, its crack propagation modeling depends on mesh reconstruction, which can introduce numerical errors and is not well suited for discontinuous material problems. The BEM reduces computational dimensions and data requirements, but its applicability is limited by modeling difficulties when addressing nonlinear problems or complex geometries. The XFEM can effectively simulate crack initiation and propagation without mesh reconstruction; however, it is highly sensitive to material parameters, becomes computationally expensive with increasing crack interactions, and struggles with complex multi-crack scenarios. Meshless Methods eliminate mesh dependency and are well suited for large deformation and multi-crack problems, yet they suffer from low computational efficiency and challenges in enforcing boundary conditions.

By contrast, the DEM, which is based on the discrete characteristics of particles, can intuitively capture the evolution of materials from micro-scale damage to macro-scale fracture. It accurately reproduces crack propagation paths, interfacial slip, and other meso-scale behaviors, offering clear advantages for modeling discontinuous deformation and complex failure modes. Although DEM faces challenges such as large computational demands and complex parameter calibration, it provides unique value in revealing the internal degradation mechanisms of materials.

In addition, studies using DEM to investigate RC have shown that factors such as aggregate shape and contact models significantly affect fatigue strength, deformation behavior, and failure patterns[16,17]. Although DEM has been increasingly applied to concrete research in recent years, publicly available studies remain limited, and investigations specifically addressing the fatigue failure mechanisms of RC are even scarcer[18,19]. Existing attempts to model RC with DEM still face several notable limitations[20,21]. First, most studies approximate coarse aggregates as spheres, which differs substantially from their actual polyhedral and irregular geometries, thereby reducing the accuracy of simulation results. Second, aggregates are typically assumed to be rigid bodies that do not fracture under load; however, in reality, aggregates can break and deform under external forces, and this simplification inevitably undermines the reliability of the simulations. Moreover, current DEM-based fatigue studies of RC rely on relatively narrow modeling approaches, often restricted to reproducing laboratory test conditions. As a result, they remain confined to macroscopic phenomenological descriptions and have yet to provide deeper insights into the intrinsic fatigue failure mechanisms of RC.

To overcome the limitations of existing DEM studies on RC, this paper employs three-dimensional scanning technology with PFC3D (Version: PFC 5.0; URL: https://www.itascacg.com/software/PFC) to construct discrete element models that capture the actual morphology of coarse aggregates. Model parameters are calibrated using prior laboratory fatigue test results on RC. Numerical four-point bending fatigue simulations are then conducted on specimens with varying corrosion rates. In parallel, acoustic emission monitoring is used to examine the relationship between strength and damage in RC bridge decks, while energy-tracking and crack-localization systems are applied to analyze load-bearing capacity, deformation, strain energy, and related responses. These investigations provide insight into the macro- and micro-mechanical processes of crack initiation and propagation under fatigue loading, thereby revealing the fatigue failure mechanisms of RC bridge decks at different corrosion levels.

Discrete element model of reinforced concrete

Three-dimensional scanning technology for block stones

The shape of coarse aggregates is a critical factor influencing the mechanical behavior of RC. Although using simplified geometric forms to represent aggregates reduces technical complexity and improves computational efficiency, this approach overlooks the irregular morphology and surface features of aggregates, making it difficult to capture their actual contact conditions, frictional behavior, and mechanical interactions with mortar or reinforcing steel. Consequently, such simplifications compromise the accuracy and reliability of simulation results. To address these limitations, several irregular particle modeling methods have been developed, including digital imaging, CT scanning, mathematical statistics, and three-dimensional scanning[22–26]. Digital image processing is primarily suited for two-dimensional simulations and is affected by particle surface reflection and lighting conditions during image acquisition, which prevent complete capture of aggregate geometry. Converting 2D images into 3D shapes often results in distortion and information loss. CT scanning, while capable of providing detailed internal structures, is costly in terms of equipment, operation, and maintenance, and has limited resolution for large aggregates due to scanning range constraints; moreover, it requires highly trained operators. Mathematical statistical methods, by contrast, are inherently "subjective" and cannot capture fine surface textures or micro-scale roughness, which are critical for simulating realistic contact and frictional interactions with surrounding materials, thereby leading to deviations between simulation and actual behavior.

In comparison, three-dimensional (3D) scanning technology can capture aggregate morphology and surface details with high precision, generating accurate 3D models. It is easy to operate, relatively low in cost, fast in scanning speed, and unaffected by spatial or environmental constraints, making it well-suited for modeling aggregates of complex shapes and providing an effective means for detailed characterization of irregular particles. However, this technology also presents certain limitations. The scanning process generates massive point

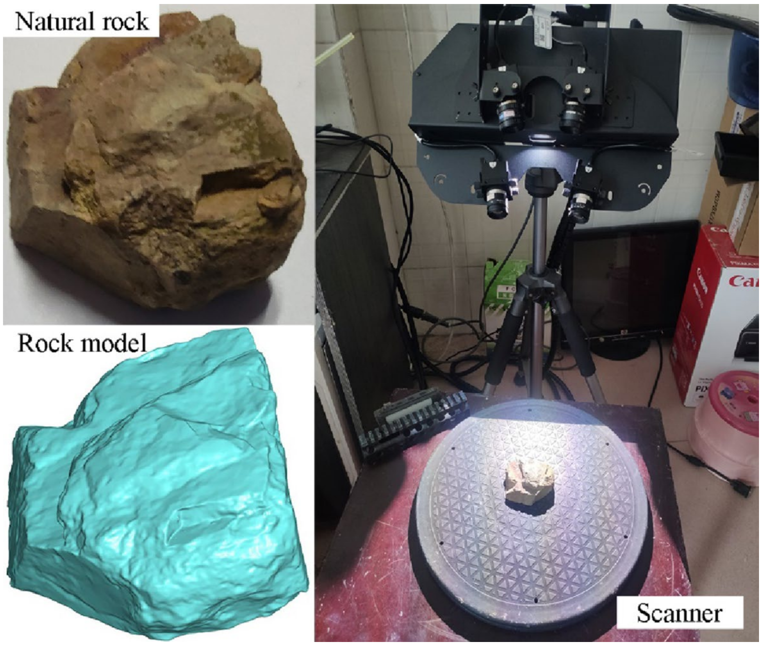

Fig. 1. Three-dimensional scanning technology for block stones.

Particle size interval/mm	5–10	10–15	15–20	20–25	25–30
Sample size	30	30	30	30	30

Table 1. Stone scanning samples.

cloud datasets, which place high demands on data storage and post-processing hardware, thereby increasing computational costs. Furthermore, post-processing techniques applied to improve model smoothness may lead to the loss of micro-scale surface roughness, ultimately affecting the accuracy of frictional behavior simulations between particles. In addition, dust, coatings, or moisture on aggregate surfaces may cause abnormal signal reflections during scanning, introducing measurement errors and reducing the accuracy of the resulting 3D models.

Despite these limitations, 3D scanning remains the most effective approach for constructing discrete element models that capture the actual morphology of aggregates in mechanical behavior studies, owing to its unmatched capability in geometric reconstruction. In this study, we mitigate the technique's inherent constraints by optimizing data-processing algorithms and improving sample preparation, thereby reducing methodological drawbacks while fully leveraging its advantages in modeling irregular aggregate geometries.

Building on the considerations above, this study combines three-dimensional (3D) scanning with stochastic aggregate placement to construct discrete element models of RC using PFC3D. To account for the variability of aggregate shapes and improve simulation accuracy, coarse aggregates with particle sizes of 5–30 mm were first selected from concrete specimens as scanning samples. These aggregates were scanned using a quad-lens 3D scanner (GD-3dscanner, Nanyang Mengyang Machinery Co., Ltd.), as shown in Fig. 1. The non-contact surface scanner provides an accuracy of 0.001–0.05 mm, a single-surface scan speed of 1–3 s, and an average point spacing of 0.015–0.1 mm. The resulting models closely approximate the actual aggregates, featuring smooth surfaces, and the scans can be exported in STL, DXF, VRML, and other formats, allowing broad applicability. During scanning, the aggregates were categorized into five particle size ranges to represent their contribution to the overall concrete mix. The number of scanned aggregates for each size range is listed in Table 1, forming a comprehensive aggregate database for subsequent modeling.

Constructing a random discrete element model

To replicate the indoor four-point bending test, the cross-sectional dimensions of the RC bridge deck model were set to 3000 mm × 400 mm × 240 mm. Following the recommendation of Wang et al.[18] regarding the coarse/fine aggregate threshold for discrete element concrete models, a threshold of 5 mm is adopted in this study. Aggregates larger than 5 mm are defined as block stones, while those smaller than 5 mm are classified as sand. Considering the grading of coarse aggregates, the Monte Carlo method is employed, and the *Clump distribute bin* command in PFC3D is used to randomly select the appropriate number of block stones from different particle size intervals in the aggregate database according to the preset grading, which are then randomly dropped into

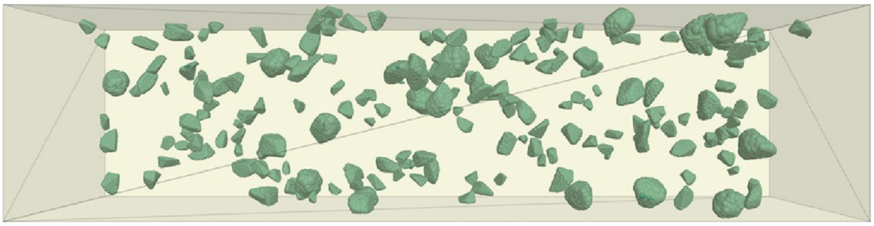

Fig. 2. Discrete element random model of stone clusters.

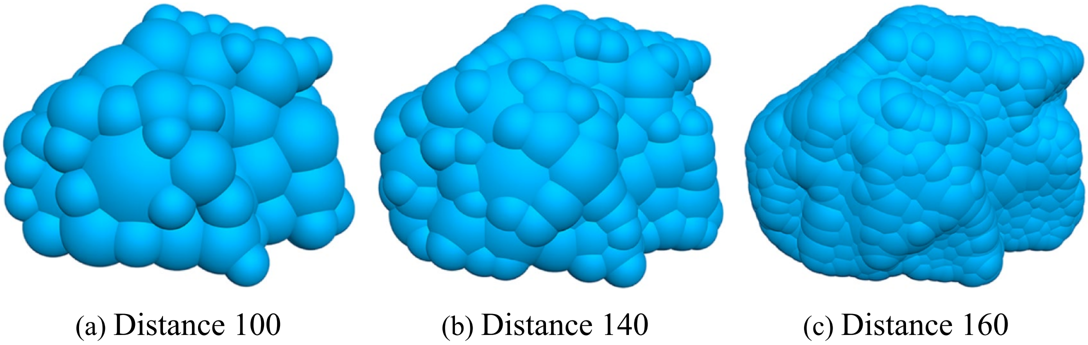

Fig. 3. Block stone models with different distance values. (**a**) Distance 100, (**b**) Distance 140, (**c**) Distance 160.

the designated region. This procedure establishes a stochastic discrete element model of block stone particle clusters, as shown in Fig. 2.

When constructing 3D scanned aggregate cluster models in PFC3D, the *Geometry import* command was first employed to import the STL digital files of the scanned aggregates. The *Clump template create* command was then applied to generate irregular particles based on the customized geometries, followed by the *Bubblepack* subcommand to fill these particles with internal Pebble elements. In PFC3D, the *Distance* command controls the number of Pebble elements used to fill the irregular model. A larger *Distance* increases the filling density and overlap of the Pebble elements, thereby enhancing the fidelity of the reconstructed model but reducing computational efficiency. Conversely, a smaller *Distance* results in fewer Pebble elements and lower model fidelity, while improving computational efficiency, as illustrated in Fig. 3. Previous studies have demonstrated[18,27,28] that in similar DEM simulations, setting the *Distance* parameter within the range of 100–160 leads to variations in model fidelity and computational efficiency but does not significantly influence the key structural response outputs.

In PFC3D, the block stone model generated using the *Clump distribute* command is represented as a rigid cluster. Such a cluster consists of multiple Pebble elements that move together as a rigid body, without relative deformation among the internal particles. Consequently, rigid clusters cannot undergo damage. However, in real engineering applications, the particle size disparity between block stones and cement mortar, as well as the inherent porosity of concrete, leads to limited contact surfaces between particles. The contacts are predominantly point-to-point. Under external loading, these point contacts easily induce stress concentrations, which may cause block stones to fracture. Once fractured, the resulting fragments are smaller and morphologically different from the original particles. This breakage alters the aggregate gradation, significantly modifying the mechanical characteristics of the material and ultimately compromising the safety and serviceability of RC bridge decks. Therefore, capturing the particle breakage behavior of block stones is essential for an in-depth investigation of fatigue failure mechanisms in RC slabs.

Rigid clusters, however, are inherently incapable of reproducing such phenomena, as they cannot account for deformation, friction, crack propagation, or particle crushing. To overcome this limitation, several modeling strategies have been proposed for simulating particle fragmentation, including the FEM, the Fragment Replace Method (FRM), and the Bonded-Particle Method (BPM). Among these, BPM has emerged as one of the most effective approaches. In BPM, a disk or sphere is considered the smallest indivisible unit, which cannot undergo further breakage. A collection of these units is bonded together to form a macro-particle. When the stress applied to a macro-particle exceeds the bond strength, particle breakage occurs, as schematically illustrated in Fig. 4 From a micromechanical perspective, BPM not only captures the macroscopic mechanical behavior of block stones but also enables the simulation of complex particle interactions, making it a suitable method for investigating fatigue-related damage in RC bridge decks.

Therefore, as shown in Fig. 5, on the basis of generating irregular block-stone rigid clumps via the Monte Carlo method, this study employs the BPM in PFC3D to simulate crushable random polygonal aggregates. First, the *Clump.pebblelist* command was used to traverse all Pebble elements within the rigid clumps, and the *Clump.pebble.radius* and *Clump.pebble.pos* commands were applied to record the radii and coordinates of the

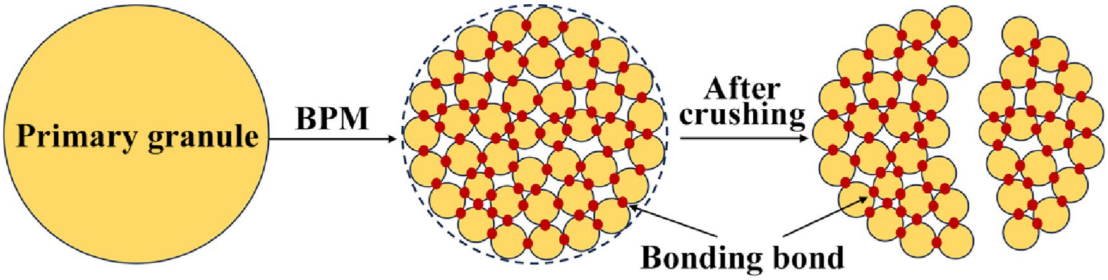

Fig. 4. Schematic diagram of particle fragmentation by bonded particle method.

Pebbles. Next, based on this Pebble information, the *Ball create* command was used to generate Ball elements that completely replace the Pebbles. Then, the Contact.prop command was applied to assign contact properties to the Ball elements, thereby forming flexible cluster particles (Clusters). Finally, the *Clump.delete* command was used to remove all rigid clump particles, as illustrated in Fig. 5. It should be noted that in simulating the fracture of flexible clusters, excessive overlap among the Balls should be avoided; otherwise, bond breakage may release unrealistically high energy, leading to distorted computational results. Therefore, taking into account both computational efficiency and accuracy in RC fatigue simulations with different Distance values, this study adopts Distance = 100.0 for modeling irregular aggregates. This parameter achieves a balanced trade-off between capturing aggregate irregularity and ensuring computational efficiency, while reliably reproducing the mechanical behavior of RC slabs.

Due to the high rigidity and ductility of steel bars, both properties must be considered when establishing a discrete element model of reinforcement. Based on these characteristics, this study generates the steel bar skeleton structure using multiple mutually independent, bonded, and regularly arranged Ball particles, as illustrated in Fig. 6. In this model, only longitudinal reinforcement is incorporated, while distributed reinforcement is omitted. The rationale is that the primary objective of this study is to investigate the critical role of longitudinal reinforcement in governing the mechanical behavior and damage evolution of the structure under fatigue loading. To more clearly reveal the fatigue damage mechanism of longitudinal reinforcement, a simplified modeling approach is adopted. Since longitudinal reinforcement bears the majority of stress under fatigue loads, whereas distributed reinforcement has only a minor influence on fatigue damage, neglecting distributed reinforcement does not significantly affect the analysis of fatigue failure mechanisms in RC slabs. Moreover, introducing distributed reinforcement would substantially increase model complexity, leading to higher computational costs, longer simulation times, and a greater potential for errors. Therefore, the simplified model represents a balanced trade-off between computational efficiency and structural fidelity, enabling a clearer focus on the key factors while enhancing the robustness and reliability of the results.

In order to further improve computational efficiency, sand particles are assumed to be spherical without compromising the accuracy of the results. After constructing the flexible cluster model of block stones and the reinforcement model, the *Ball distribute bin* command is used to generate simulated sand with a particle size range of 0–5 mm according to the prescribed grading, which is then used to fill the voids between coarse aggregates, as shown in Fig. 7. When establishing a random discrete element model of concrete, several additional steps are required to ensure close particle contact. First, the radius of spherical particles is temporarily reduced to 0.01 times the original size to generate a pure sand model. Next, the overlapping portions with the block stone and reinforcement models are removed. The *Porosity* command is then applied to regulate sample porosity and prevent excessive deletion or retention of spherical particles. Finally, the remaining particles are restored to their original size, and the Cycle command in PFC3D is executed for a specified number of steps to adjust particle orientations. This process ensures tight packing of particles, drives the system toward equilibrium, and guarantees both numerical stability and accuracy of the simulation outcomes.

Contact model selection and parameter calibration

In this study, the parallel bond model in PFC3D was adopted as the particle contact model to account for the bonding effects between RC particles. This model more accurately represents the tensile and bending behavior of the material, whereas the contact between the loading plate and the specimen was modeled using a linear contact model[29]. The linear model was chosen for its computational efficiency and its ability to simulate the elastic contact behavior between the loading plate and the specimen, making it suitable for ensuring rapid force updates and stable contact interactions under cyclic loading.

Furthermore, several critical nonlinear mechanisms were considered, including the opening and closing of discrete cracks in RC, interactions between steel bars and concrete, frictional sliding between cement mortar and coarse aggregates, localized plastic deformation and misalignment of steel bars under cyclic loading, and the mechanical behavior of Pebble particles within block stones. These mechanisms are essential for accurately capturing the highly nonlinear structural response under cyclic loading. Following the recommendations of Potyondy and Cundall[30] and building on our group's previous research[18], appropriate contact properties were assigned to different particle types, as illustrated in Fig. 8, Table 2. Since the interfacial transition zone represents the weakest region of the structure, the contact stiffness between dissimilar material particles was set lower than that between cement mortar particles. Although two contact models were employed in PFC3D, distinct contact parameters were defined for block stone–cement mortar, block stone–steel bar, cement mortar–steel

(a) Experiment

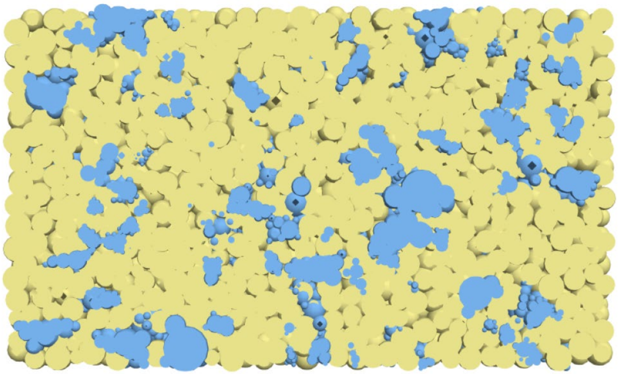

(b) Simulation

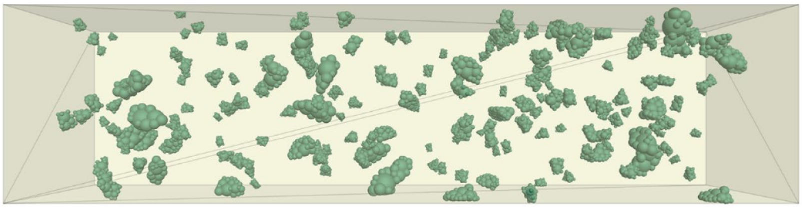

(c) Clump model of random block stones.

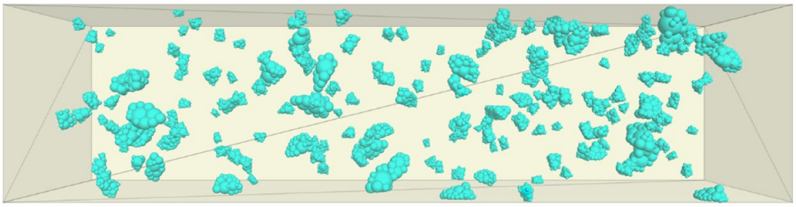

(d) Cluster model of random block stones.

Fig. 5. Discrete element model considering the crushing effect of block stones. (**a**) Experiment, (**b**) Simulation, (**c**) Clump model of random block stones, (**d**) Cluster model of random block stones.

bar, steel bar ball–steel bar ball, cement mortar ball–cement mortar ball, and block stone pebble–block stone pebble interactions. This differentiation ensures that the discrete element model of RC remains consistent with established mechanical theory, thereby improving both the reliability and accuracy of the simulation results.

The mechanical properties of the discrete element model are governed by the microscopic parameters of the particles. In this study, the range of these microscopic parameters was determined by integrating the results of the RC fatigue tests. By fine-tuning the parameter values, the calibration process was considered complete once the simulation results achieved maximum adjustable similarity with the experimental data.

The indoor RC fatigue tests were conducted using a large-scale fatigue loading machine developed by Fuzhou University. The arrangement of concrete and steel strain measurement points for the RC specimens is shown

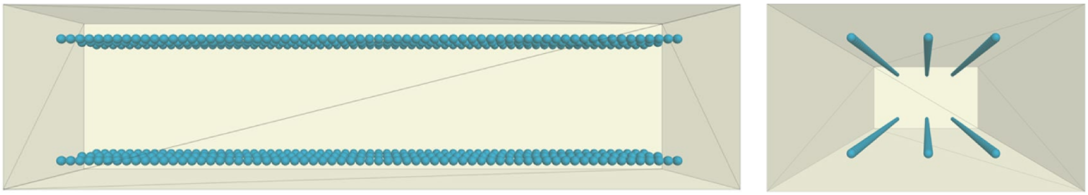

(a) Front view of reinforcement. (b) Side view of reinforcement.

Fig. 6. Steel bar spatial structure. (**a**) Front view of reinforcement, (**b**) Side view of reinforcement.

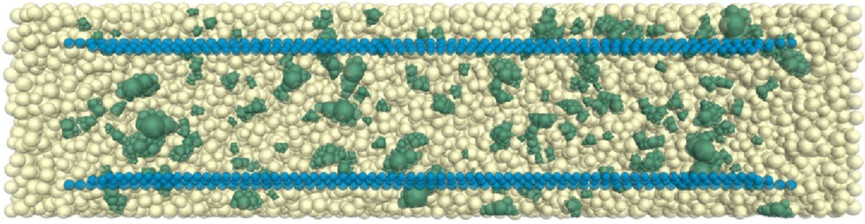

Fig. 7. Random discrete element model of RC.

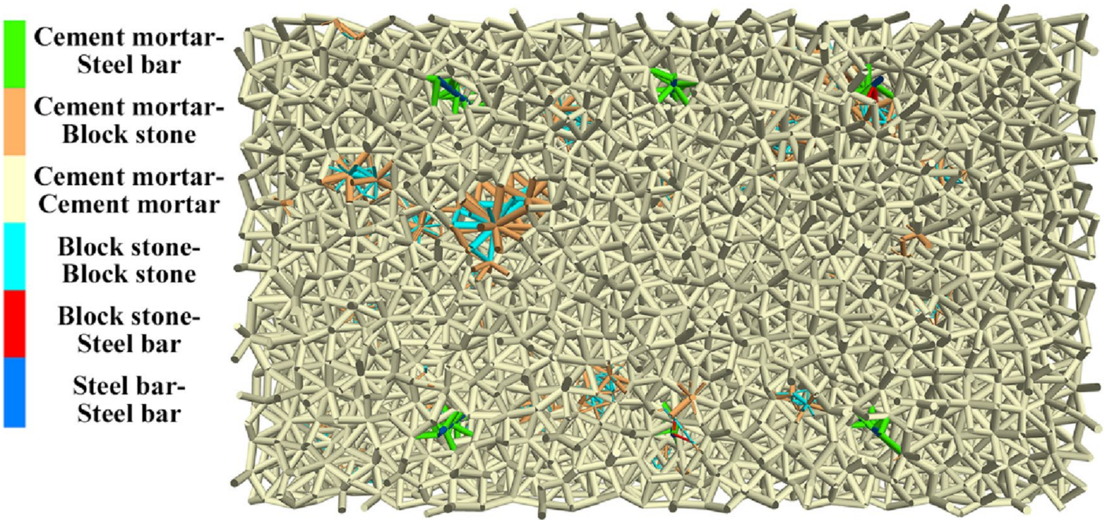

Fig. 8. Contact and bond distribution of RC.

Parameter category	Effective modulus/GPa	Stiffness ratio	Friction coefficient	Parallel bond friction angle/°	Parallel bond tensile strength/MPa	Parallel bond cohesion/MPa
Block stone	2.05e2	1.2	0.6	40	38	26
Steel bar	3.23e3	1.2	0.5	49	2.35e2	2.35e2
Cement mortar	98	1.0	0.4	32	4.5	9.2
Block stone-cement mortar	49	1.0	0.3	18	2.9	4.2
Steel bar-cement mortar	73	1.0	0.3	25	1.8	6.0
Block stone-steel bar	23	0.7	0.55	12	0.9	2.6

Table 2. Contact model parameter values of RC.

(a) Fatigue loading test of RC.

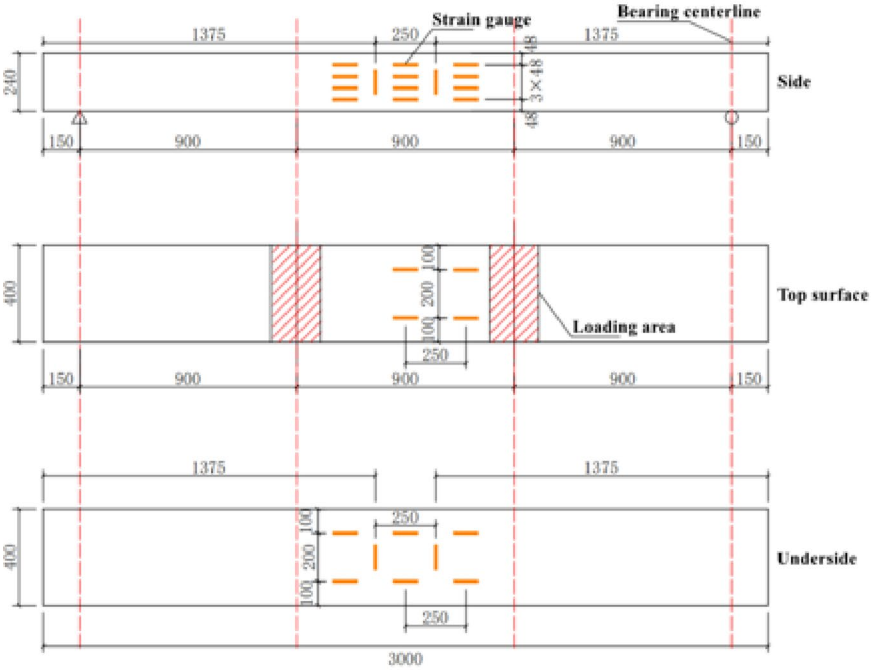

(b) Section diagram of concrete strain measuring point layout of specimen

Fig. 9. Schematic diagram of fatigue loading test of RC. (**a**) Fatigue loading test of RC. (**b**) Section diagram of concrete strain measuring point layout of specimen, (**c**) Schematic diagram of layout section of steel bar strain measuring point of specimen.

in Fig. 9. The RC specimens were designed with a concrete strength grade of C50 and reinforcement grade HRB 400. The specimen dimensions were 3000 mm × 400 mm × 240 mm, with a reinforcement ratio of 1.18%. During the fatigue loading tests, a constant-amplitude sinusoidal load was applied to the specimens. The lower limit of the fatigue load considered only the dead load effects such as the self-weight of the bridge deck, and was set relatively small at 0.1Fu. The upper load limit of the beam was set to 0.5Fu. Based on the static loading test results, the reference load Fu was determined as 500 kN. Accordingly, the lower fatigue load was set to 50 kN, the upper fatigue load to 250 kN, and the loading frequency to 10 Hz. Loading was terminated once any of the following conditions occurred: fracture of the tensile reinforcement, spalling failure of the compressed concrete in the upper zone, maximum crack width reaching 1.5 mm, or mid-span deflection exceeding 40 mm. The strength and deformation curves of the specimens are shown in Fig. 11.

This study employed the PFC3D discrete element software for numerical simulation, with computations performed on a workstation configured as follows: CPU: EPYC 9554 (64 cores/128 threads), GPU: RTX 6000 Ada 48G × 2, and memory: 32G DDR5 RECC 4800 × 8. Following the fatigue test scheme of reinforced concrete bridge deck slabs, a corresponding discrete element model was constructed in PFC3D, as shown in Fig. 10. After parameter calibration, the micro-scale contact model parameters of the materials were determined, as shown in Table 1. Both the laboratory test specimens and the numerical model underwent three million loading cycles. A comparison of the experimental and simulation results is shown in Fig. 11. As seen in Fig. 11, the simulation

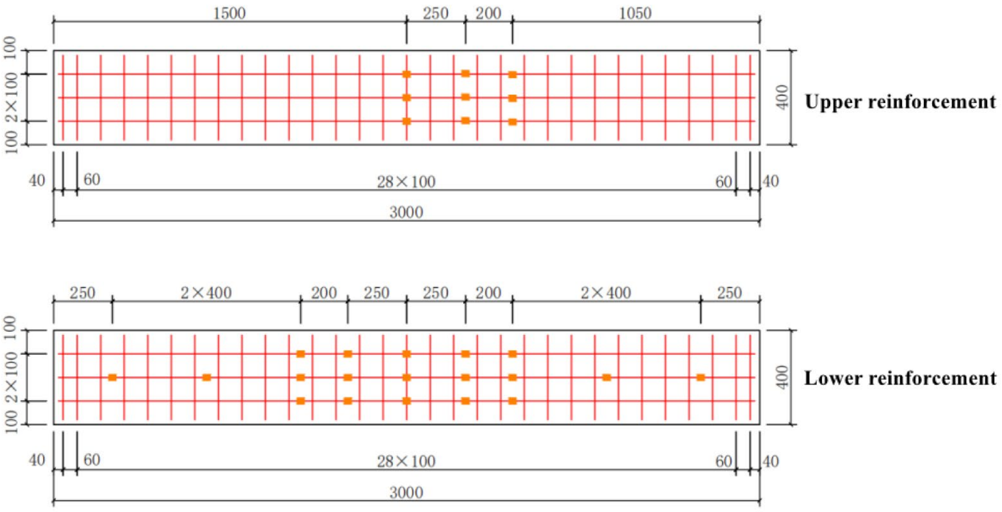

(c) Schematic diagram of layout section of steel bar strain measuring point of specimen.

Fig. 9. (continued)

curve fits the experimental curve well from the beginning of loading until material failure. According to the relative error formula, the relative error between the two is 3.7%, thereby confirming that the selected contact constitutive relationship and micro-parameters can reasonably represent the mechanical behavior of reinforced concrete slabs and provide a solid foundation for subsequent micro–macro mechanism analysis. Although the overall agreement between the simulated and experimental curves is satisfactory, a relative error of 3.7% remains. This discrepancy is primarily attributable to unavoidable factors during the physical test, such as slight fluctuations in the loading equipment and intrinsic heterogeneity of the material. By contrast, the numerical simulation is based on idealized constitutive laws and homogenized micro-parameters, which inevitably differ from actual experimental conditions and thus contribute to the observed error.

It should be noted that, although the initial ranges of micro-parameters for concrete, reinforcement, and aggregates were informed by relevant literature, the final calibration of the RC discrete element model was achieved by fitting to the macro-mechanical data obtained from four-point bending fatigue tests on RC slabs. Due to experimental constraints and time limitations, this study did not conduct independent validation tests specifically for the micro-parameters of concrete and reinforcement. Consequently, the rationality of the adopted micro-parameters was indirectly validated through consistency with findings reported in similar studies and by the degree of agreement between the macro-responses of a single set of physical tests and the numerical results. This limitation implies that the calibrated parameters may be strongly adapted to the specific specimens studied, while their general applicability across different concrete strength grades, reinforcement ratios, or loading conditions remains to be further confirmed. Future research will address these limitations by incorporating multiple sets of physical tests under varied conditions, conducting independent validation experiments, and integrating machine learning algorithms to optimize the parameter calibration process. These efforts aim to enhance the reliability of model parameters and improve the generalizability of the results.

Fatigue test simulation of corroded reinforced concrete

Based on the above experimental conditions, this chapter conducts fatigue simulation tests on reinforced concrete with mild (10%), moderate (25%), and severe (40%) corrosion, where the corrosion rate corresponds to the mass loss ratio of the reinforcement (i.e., a 10% corrosion rate indicates a 10% mass loss of the reinforcement, with 25% and 40% defined accordingly). By referencing published studies on corroded reinforced concrete, the different corrosion levels in this work are represented through adjustments of the micro-parameters listed in Table 3.

Effect of reinforcement corrosion on mechanical properties

In the fatigue tests, dynamic stiffness was used to describe the variation of RC stiffness under cyclic loading. Figure 12 shows the relationship between the stiffness ratio and the fatigue cycle ratio for RC specimens with different corrosion levels, where n is the number of cycles and N_0 is the fatigue life of the RC slab with 0% corrosion. The fatigue lives for RC slabs with 0%, 10%, 25%, and 40% corrosion are 3, 2.4, 1.86, and 1.44 million cycles, respectively. As shown in the figure, RC fatigue damage can be divided into three stages. In the initial stage, the neutral axis rises rapidly, and the stiffness ratio drops sharply, accounting for approximately 10% of

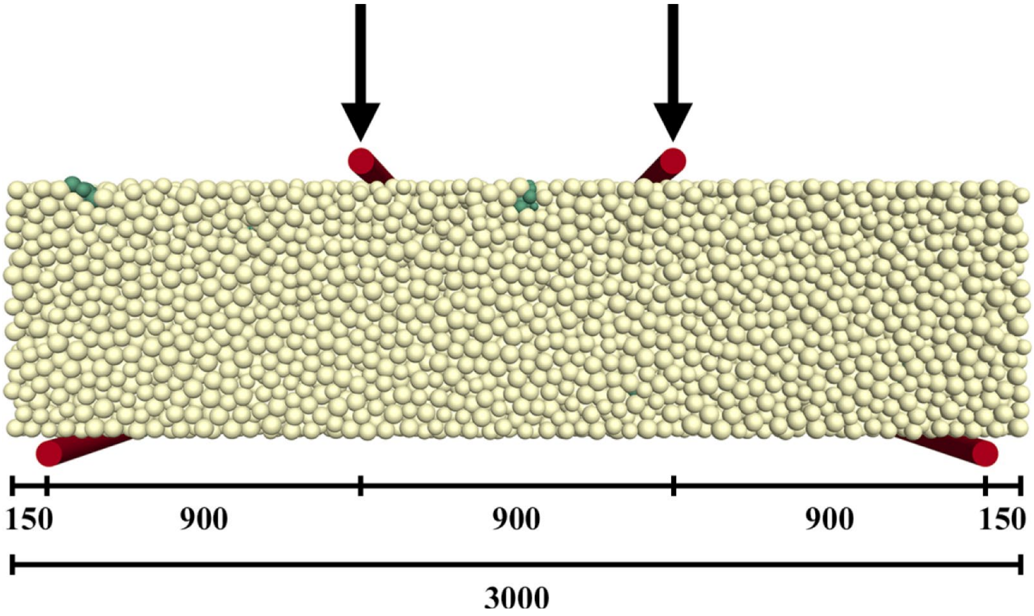

(a) Front view

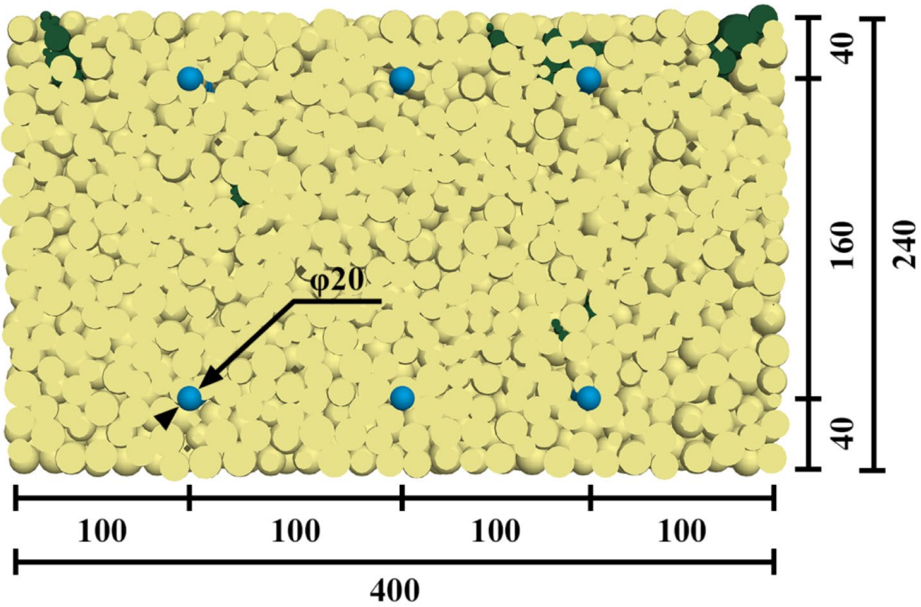

(b) Cross-sectional view

Fig. 10. Schematic diagram of fatigue load loading of RC discrete element model (Umit: mm). (**a**) Front view, (**b**) Cross-sectional view, (**c**) Loading path.

the fatigue life. In the second stage, the stiffness ratio decreases steadily due to the slow upward movement of the neutral axis, exhibiting an approximately linear relationship with the fatigue cycle ratio. In the final stage, the stiffness ratio drops abruptly, with the residual stiffness maintained by the uncrushed aggregate in the concrete compression zone, indicating that the structure has reached a critical failure state[31,32].

Furthermore, a comparison of stiffness curves reveals clear differences in degradation patterns among corrosion levels. For uncorroded specimens (0%), stiffness attenuation occurs gradually, and residual stiffness remains at about 60%. With mild corrosion (10%), rust products weaken the bond between reinforcement and surrounding concrete, thereby accelerating stiffness attenuation by approximately 41% relative to uncorroded specimens, with residual stiffness reduced to 50%. Under moderate corrosion (25%), expansion stresses from corrosion cause network cracking of the protective concrete cover, resulting in an 86% higher rate of stiffness attenuation and residual stiffness of only 46%. When corrosion is severe (40%), the reduction in effective steel area, combined with deterioration in its mechanical properties, dominates the failure process. Rust-induced expansion leads to premature peeling of the protective layer, while cyclic loading intensifies local stress

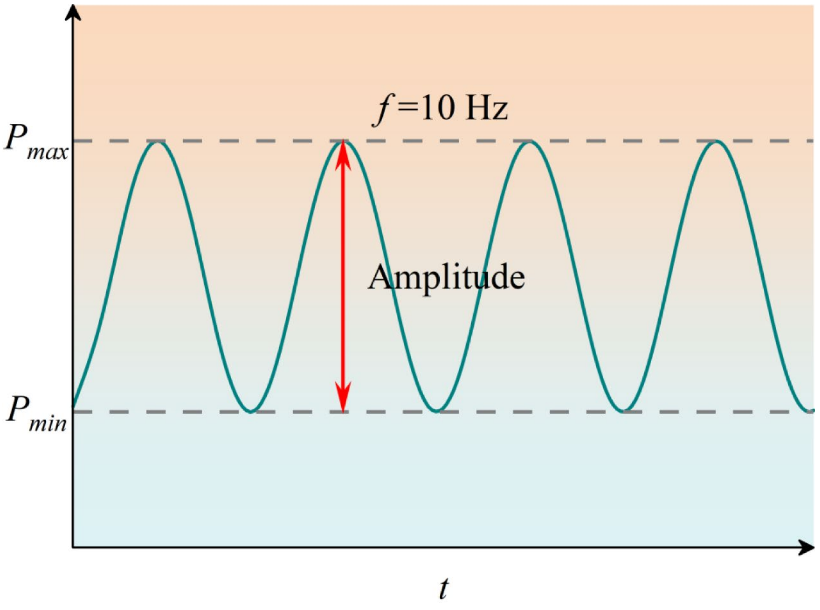

(c) Loading path

Fig. 10. (continued)

concentrations. As a result, stiffness decreases steeply during the initial cycles, and failure occurs at a cycle ratio of only 0.4, with residual stiffness falling to just 30%.

In addition to stiffness, dynamic deflection provides another critical measure of fatigue performance, as it reflects cumulative damage and indicates whether serviceability limits are exceeded. As shown in Fig. 13, deflection–cycle ratio curves follow a hierarchical, three-stage progression. At the initial elastic stage, deflection rises rapidly, driven mainly by elastic deformation. During the stable development stage, deflection accumulates slowly in a nearly linear fashion, representing more than 90% of the fatigue life. In the final accelerated failure stage, deflection increases sharply and nonlinearly until collapse, at which point reinforcement yielding and concrete crushing interact, leading to total loss of structural bearing capacity.

Moreover, corrosion is found to exacerbate deflection development significantly. For uncorroded specimens (0%), the curve is relatively flat, with residual deflection of 4.5 mm and failure deflection of 11.0 mm. At 10% corrosion, the slope of the curve increases by 53%, residual deflection rises by 11%, while failure deflection decreases slightly (−2.5%). At 25% corrosion, the specimens exhibit pronounced brittleness, with residual deflection reaching 6.5 mm (1.6 times higher than uncorroded specimens) and failure occurring earlier, with deflection reduced by 10.5%. Finally, at 40% corrosion, deflection grows dramatically, and fracture occurs at a cycle ratio of only 0.5. Residual and failure deflections are 8.0 mm and 9.1 mm, accounting for 78% and −17% of uncorroded values, respectively.

Taken together, these observations point to a clear mechanism: corrosion deteriorates the RC skeleton and forces reconstruction of the load-transfer path[7,33]. In uncorroded specimens, stiffness is maintained primarily by the intact aggregate–mortar skeleton and the strong steel–concrete bond, while aggregate interlock ensures efficient stress transfer, thereby slowing the upward movement of the neutral axis. Once corrosion occurs, however, rust-induced expansion cracks the protective concrete cover, weakens aggregate–mortar bonding, and increases aggregate slip and rotation, all of which accelerate stiffness loss.

As corrosion progresses, two additional effects of rust at the steel surface further undermine performance. First, expansion cracking disrupts aggregate interlock, and under cyclic loading, aggregates break and rearrange, sharply reducing stiffness. Second, loss of steel cross-section and surface roughening intensify stress concentrations, fostering localized slip bands at the steel–concrete interface. These changes shift load transfer from uniform global coordination to localized concentration. At severe corrosion (40%), these mechanisms interact: steel section loss and cover spalling alter the stress-bearing skeleton, crushed aggregates disrupt continuity in the compression zone, and multiple plastic hinges form in the tensile reinforcement. Consequently, the load path is forced to redistribute around cracked zones, manifesting as a cliff-like stiffness drop and rapid deflection surge.

In conclusion, RC slabs with higher levels of corrosion exhibit both greater stiffness degradation and accelerated deflection growth under fatigue loading. These responses directly reflect the profound structural damage induced by reinforcement corrosion, undermining not only the load-bearing capacity but also the long-term durability of the structure.

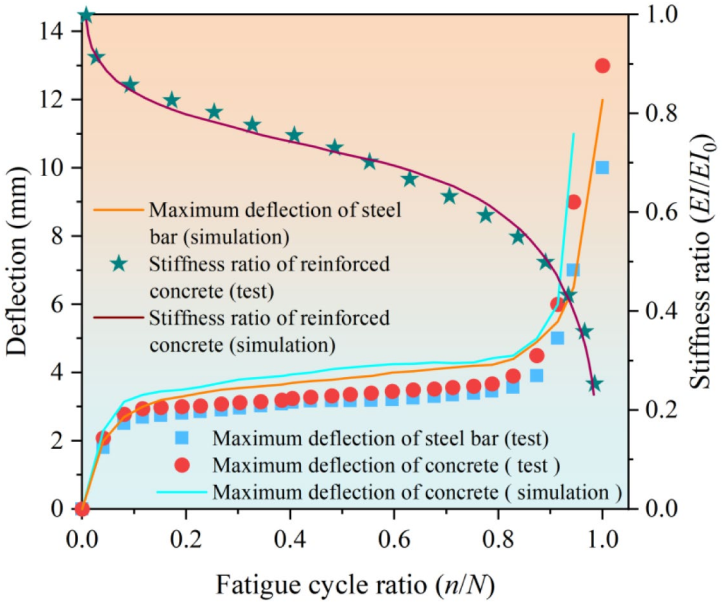

(a) Comparison of test and simulation curves

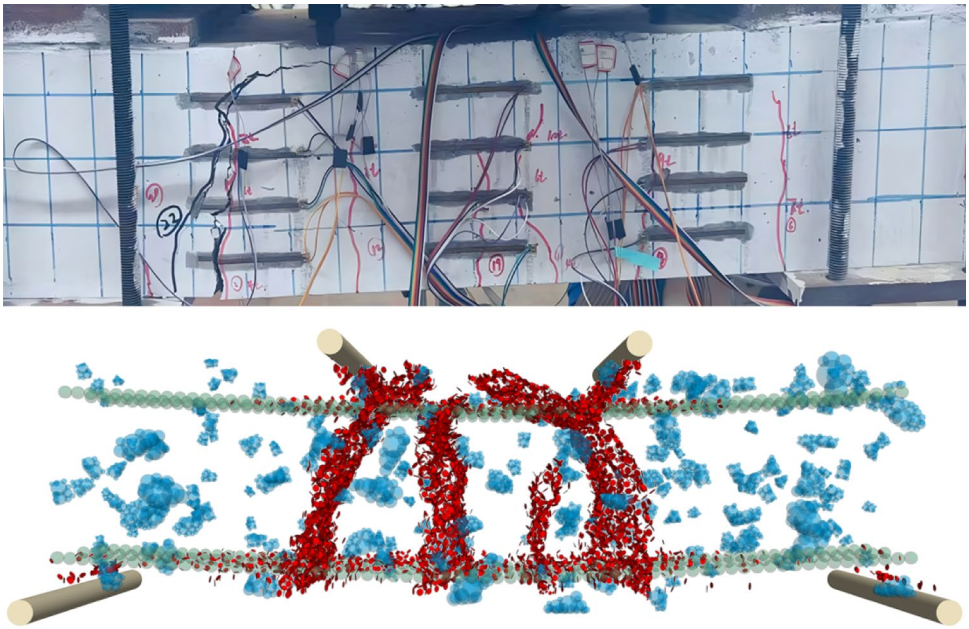

(b) Comparison of test and simulated failure modes

Fig. 11. Fatigue test results of RC. (**a**) Comparison of test and simulation curves, (**b**) Comparison of test and simulated failure modes.

Analysis on fatigue damage process of corroded reinforced concrete

In the fatigue loading test, the RC slab ultimately failed due to crushing of the concrete at the top of the midspan. Meanwhile, the numerical simulation provided a more detailed description of the progressive damage distribution throughout the loading process. To systematically analyze the internal structural damage mechanisms of corroded RC slabs under fatigue loading, this section employs PFC3D to investigate the failure process from a microscopic perspective.

To more accurately identify the spatial orientation of microcracks, tensile strength and cohesion are defined as the critical thresholds for tension- and shear-induced cracking. Once the local stress exceeds these thresholds, the interparticle bond between balls breaks, leading to the initiation of either tensile or shear cracks. Given the large volume of data and the similarities in crack development patterns, the following analysis focuses on uncorroded RC slabs as a representative case to examine the microscopic fatigue failure mechanism. The failure process is illustrated in Fig. 14.

Corrosion degree/%	Parameter category	Effective modulus/GPa	Stiffness ratio	Friction coefficient	Parallel bond friction angle/°	Parallel bond tensile strength/MPa	Parallel bond cohesion/MPa
0	Steel bar	3.23e3	1.2	0.5	49	2.35e2	2.35e2
	Cement mortar	98	1.0	0.4	32	4.5	9.2
	Steel bar-cement mortar	73	1.0	0.3	25	1.8	6.0
10	Steel bar	3.0e3	1.1	0.45	45	2.0e2	2.0e2
	Cement mortar	90	0.9	0.35	30	4.0	8.0
	Steel bar-cement mortar	65	0.9	0.25	22	1.5	5.0
25	Steel bar	2.7e3	1.0	0.4	40	1.7e2	1.7e2
	Cement mortar	80	0.8	0.3	28	3.5	7.0
	Steel bar-cement mortar	55	0.8	0.2	20	1.2	4.0
40	Steel bar	2.4e3	0.9	0.35	35	1.4e2	1.4e2
	Cement mortar	70	0.7	0.25	25	3.0	6.0
	Steel bar-cement mortar	45	0.7	0.15	18	1.0	3.0

Table 3. Contact model parameter values for reinforced concrete with varying corrosion levels.

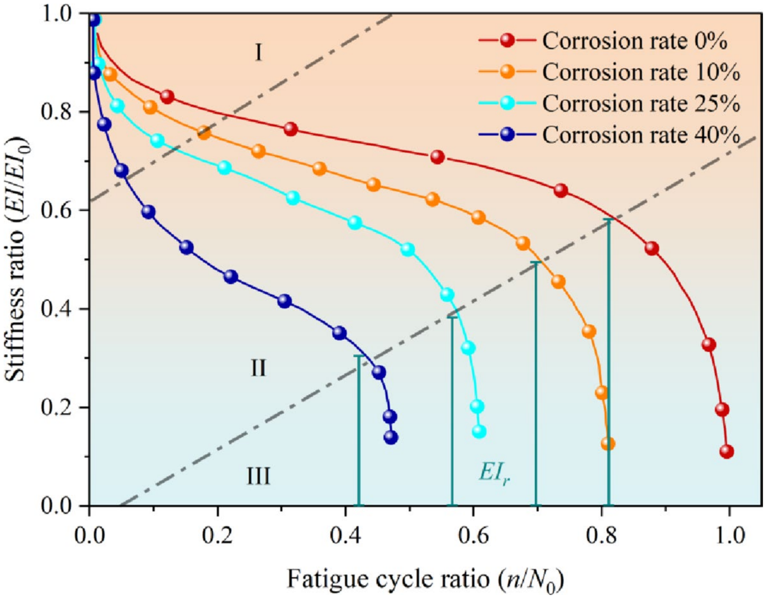

Fig. 12. Curve between stiffness ratio and cycle ratio.

As shown in Fig. 14, the fatigue damage evolution of RC slabs can be divided into three distinct stages:

Crack Initiation Stage. At the early stage of loading, microcracks first emerge at stress concentration points, namely the supports and loading locations. Subsequently, flexural cracks initiate in the pure bending zone between the loading points and gradually extend into the compression zone. During this process, cracks propagate upward from the protective layer of the reinforcing bars toward the upper concrete, forming a nearly vertical crack band. These initial microcracks primarily localize around the interfacial transition zone (ITZ), which represents the weakest link between materials.

Stable Crack Propagation Stage. With the accumulation of load cycles, plastic damage within the slab intensifies. Bond slip develops between the reinforcing bars and the surrounding concrete, and the strain in the steel evolves nonlinearly. Microcracks gradually extend from the tensile zone into the compression zone and evolve into inclined cracks directed toward the loading point. Within the mortar matrix, cracks typically propagate in straight paths; however, some are deflected along the surfaces of coarse aggregates. A small proportion of cracks also penetrate aggregates, leading to particle breakage and secondary cracking, which demonstrates the structure's inherent ductility. During this stage, microcracks cluster and coalesce, increasing crack width and length while reducing crack spacing. The primary fracture path begins to form, while non-dominant cracks either slow their growth or cease propagation. This stage is the longest of the three, comprising approximately 90% of the slab's total fatigue life.

Crack Instability Stage. Eventually, the microcracks in the protective layer form an interconnected crack network. The dominant cracks then extend until they traverse the entire section. Slip and peeling occur between

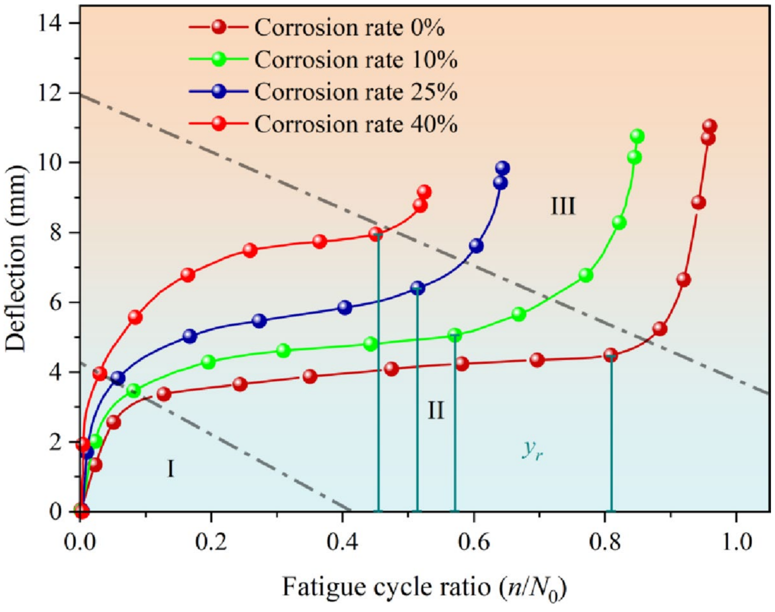

Fig. 13. Curve between deflection and cycle ratio.

the reinforcing bars and the surrounding concrete, with microcracks concentrated around the reinforcement—exceeding 80% in the tensile zone and 70% in the compression zone. A continuous slip band develops, with a width approximately equal to the reinforcing bar diameter, and the slip distribution exhibits a gradient pattern. Although the reinforcement yields, it does not fracture, while the concrete in the compression zone crushes. The failure mode is governed by shear–compression mechanisms, accompanied by a progressive increase in midspan deflection and a reduction in flexural rigidity.

The above microscopic description aligns closely with particle-scale mechanics. Specifically, during the initiation stage, stress concentration near loading and support points increases the contact forces between particles in the mortar and aggregates. Because the ITZ is relatively weak, repeated loading causes its bonds to break first, leading to the initiation of microcracks. Tensile stresses from bending exceed the bond strength in the lower pure bending region, generating additional cracks that extend upward into the compression zone.

As fatigue loading progresses into the stable propagation stage, the relative displacement between the steel reinforcement and surrounding concrete particles increases, producing bond slip. Coarse aggregates begin to rotate and slide within the mortar matrix, while stress-induced bond breakage in the mortar allows cracks to extend linearly. Some cracks deviate around aggregates due to particle interactions, while others penetrate aggregates once their strength threshold is surpassed. Fragmentation of aggregates produces fine particles that temporarily bridge cracks, delaying propagation but simultaneously generating new stress concentrations that cause secondary cracking. Ultimately, microcracks cluster into dominant fracture paths, while non-dominant cracks are suppressed due to stress redistribution.

Upon entering the instability stage, two critical transformations occur. First, the topological structure of aggregate particle groups is disrupted, and the coordination number within the tensile zone decreases, undermining mechanical continuity. Second, large-scale peeling occurs at the steel–concrete interface, manifested as bulk displacement of the surrounding concrete particle group. Fine particles produced by aggregate crushing accumulate in the slip zone, forming a fluid-like layer that drastically reduces interfacial shear strength. In the compression zone, damage develops through a cascading aggregate-crushing effect, where the fracture of a single particle induces successive failures in adjacent particles. This mechanism produces an inclined fracture zone, the orientation of which corresponds to the macroscopic shear cracks observed. Such cross-scale consistency confirms that fatigue failure in RC is essentially a process of progressive particle-system instability.

Figure 15 presents the crack distributions for RC slabs with different corrosion rates. Comparative analysis reveals that:

Uncorroded specimens exhibit ductile bending failure with typical M-shaped cracks at 45° oblique sections. The reinforcement yields but does not fracture, and local peeling of the protective layer occurs. A total of 6921 microcracks form, concentrated near reinforcement and along the crack paths.

At 10% corrosion, the failure mode shifts to a mixed bending–shear type, characterized by *N*-shaped cross cracks and significant necking of the reinforcement. The number of microcracks decreases to 5882, with dense slip zones forming around ribbed reinforcement.

At 25% corrosion, the slabs display brittle shear failure[34,35]. *Y*-shaped main cracks dominate, while the bond between steel and concrete weakens markedly. Aggregate fracture accelerates, stress redistributes, and interface bond strength declines. A total of 5744 microcracks form, accompanied by uneven deformation and prominent brittleness.

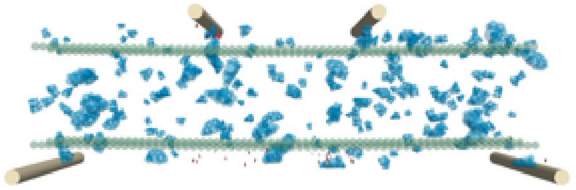

(a) ε=0.005

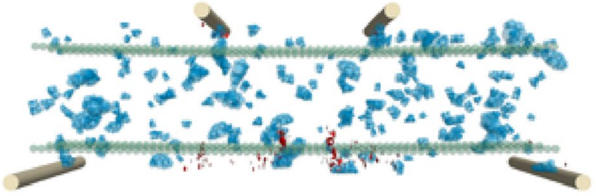

(b) ε=0.05

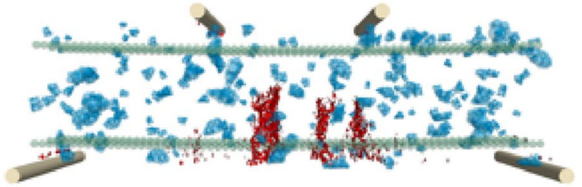

(c) ε=0.24

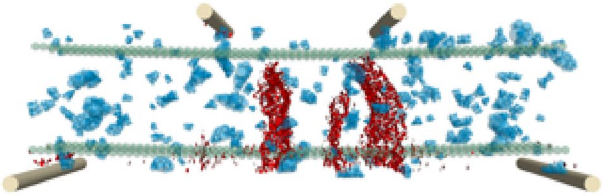

(d) ε=0.69

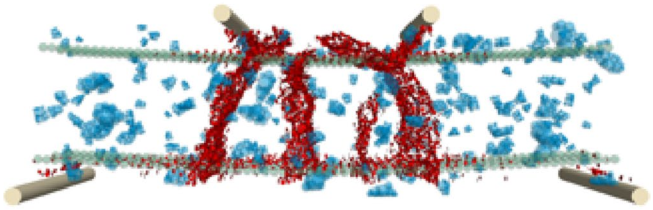

(e) ε=0.95

Fig. 14. Crack evolution process of uncorroded reinforced concrete slab under fatigue load. (**a**) $\varepsilon = 0.005$, (**b**) $\varepsilon = 0.05$, (**c**) $\varepsilon = 0.24$, (**c**) $\varepsilon = 0.69$, (**d**) $\varepsilon = 0.95$.

At 40% corrosion, sudden splitting failure occurs[36,37]. Multiple reinforcement fractures and severe aggregate breakage are observed, with *H*-shaped crack networks forming. At this stage, 5,542 microcracks are recorded, and the failure mode is characterized by catastrophic brittle shear.

In summary, the variation in fatigue failure modes with increasing corrosion is primarily governed by the coupled degradation of interface properties and evolving micromechanical behavior. For uncorroded specimens, ductile bending failure results from effective ITZ integrity, strong mortar–aggregate interlock, and stable aggregate rotation (limited to 5°), producing a controlled *M*-shaped crack path. At 10% corrosion, increased bar surface roughness and reduced rib interlock efficiency promote *N*-shaped cracks, while ITZ deterioration accelerates microcrack growth and protective layer damage. At 25% corrosion, brittle behavior emerges due to three concurrent mechanisms: decreased steel yield strength causing strain localization, higher aggregate fracture rates driving stress redistribution, and diminished bond strength altering load transfer paths. The aggregate rotation angle sharply increases, resulting in *Y*-shaped cracks. At 40% corrosion, bar area reduction and severe aggregate fragmentation amplified brittleness. Fine particles generated by aggregate crushing created a "ball-bearing effect" that lowered interfacial friction, while increased ITZ porosity accelerated crack propagation, culminating in *H*-shaped splitting failure.

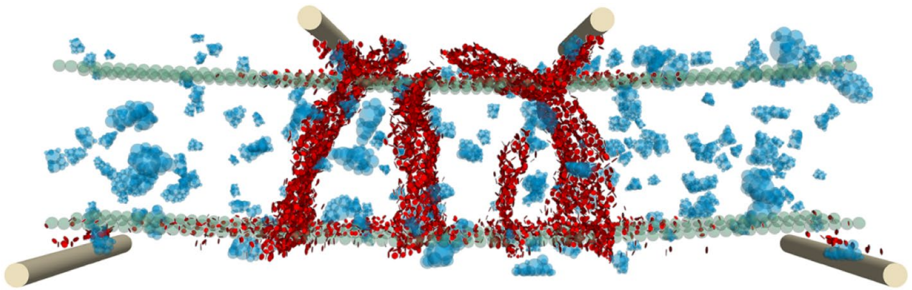

(a) Corrosion rate 0%

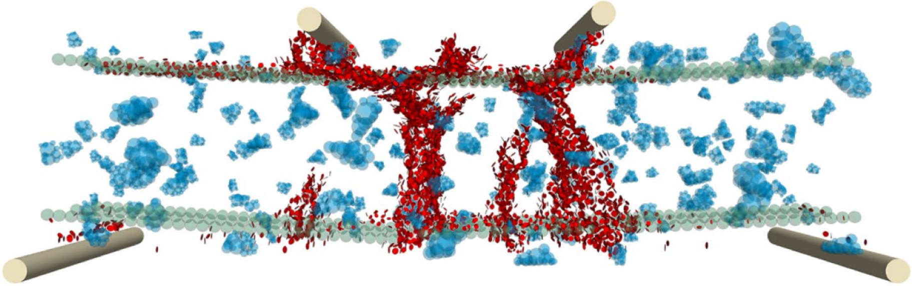

(b) Corrosion rate 10%

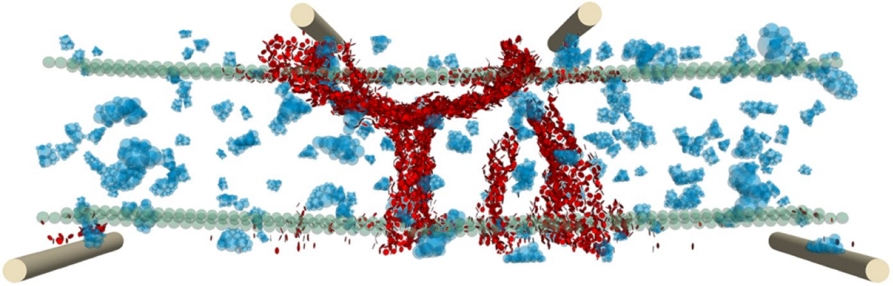

(c) Corrosion rate 25%

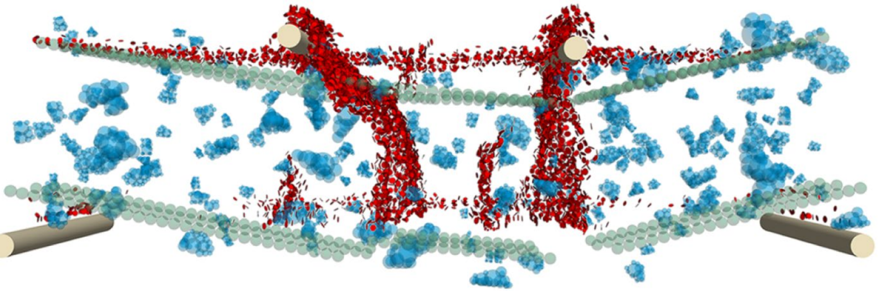

(d) Corrosion rate 40%

Fig. 15. Crack location image of reinforced concrete slab after failure under fatigue load. (**a**) Corrosion rate 0%, (**b**) Corrosion rate 10%, (**c**) Corrosion rate 25%, (**d**) Corrosion rate 40%.

It is noteworthy that the decreasing total number of microcracks across corrosion stages (6921 → 5882 → 5744 → 5542) reflects a fundamental shift: with corrosion, damage evolves from a "many and fine" distributed-crack pattern to a "few and wide" concentrated-crack mode. This transition highlights the dual role of interface degradation and aggregate skeleton collapse in driving the fatigue failure of RC slabs.

Analysis of acoustic emission characteristics during fatigue failure

At present, acoustic emission (AE) analysis is widely used to study fatigue damage and fatigue behavior in various materials and structures. Noorsuhada[38] provided a comprehensive review and assessment of AE-based studies on fatigue damage in reinforced concrete structures, showing that AE is valuable for identifying stress-induced cracks, corrosion, fracture propagation, and large crack development, thereby supporting early damage detection and prioritization of maintenance. AE data primarily include parameters such as energy and event counts, where energy reflects the development of internal defects in reinforced concrete, and event counts characterize the material's damage level. In this section, based on our research group's previous discrete element AE simulation methods[18,39], acoustic emission and strain energy monitoring techniques are employed to investigate the deformation and failure processes of reinforced concrete slabs under fatigue loading. By analyzing the damage states at different stages, the deformation–failure mechanism of the slabs is revealed.

Figure 16 shows that AE activity during fatigue failure follows a clear pattern, allowing the process to be divided into three stages[40–43]: Stage I—microcrack initiation, Stage II—stable crack development, and Stage III—rapid crack propagation leading to structural instability.

Stage I: In the initial phase, both AE event counts and strain energy exhibit relatively high activity, although their growth rates gradually decline with time. As reinforcement corrosion intensifies, both indicators show downward trends, with maximum reductions of approximately 35%. The largest observed variations in AE event counts are 65, 33, 55, and 36, while corresponding variations in strain energy rates reach 300, 270, 312, and 462. Overall, Stage I constitutes about 10% of the total fatigue life.

Stage II: During the second stage, AE activity drops to roughly 50% of the values recorded in Stage I, while the strain energy growth rate stabilizes, indicating steady microcrack development. Microcrack propagation slows considerably in this phase. Moreover, differences in AE and strain energy responses among specimens with varying corrosion levels become increasingly evident. As corrosion rate increases, AE event counts decrease, with average values of 20, 21, 24, and 27, while strain energy decreases by approximately 40%. Stage II is the longest phase, representing nearly 70% of the fatigue life.

Stage III: In the final stage, both AE event counts and strain energy undergo abrupt changes. AE activity rises sharply, with increases of up to 60%, while strain energy reaches a peak before declining. The rate of this decline varies with corrosion severity: higher corrosion rates correspond to lower peak strain energies, measured at 432, 395, 215, and 98 N·m, respectively. The downward trend becomes more pronounced with greater corrosion damage. Stage III typically accounts for about 20% of the fatigue life.

The above phenomena can be explained by both macroscopic and microscopic factors. From a macroscopic perspective, reinforced concrete initially behaves elastically under fatigue loading. External loads deform the

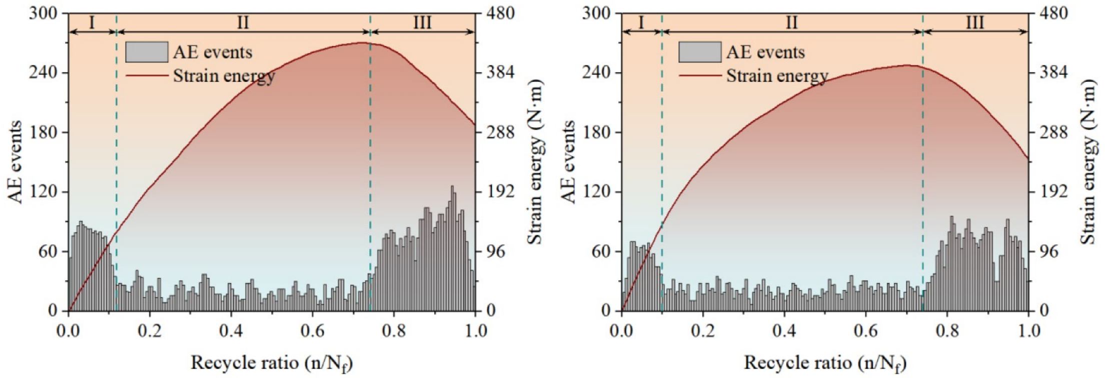

(a) Corrosion rate 0%

(b) Corrosion rate 10%

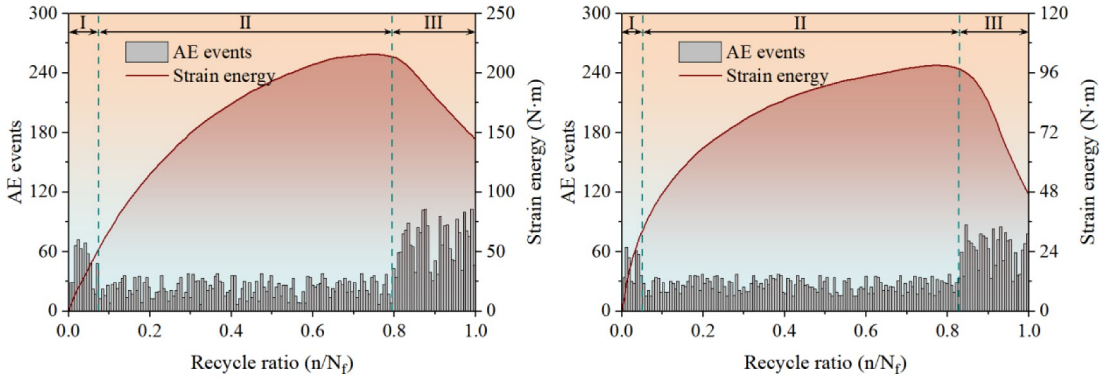

(c) Corrosion rate 25%

(b) Corrosion rate 40%

Fig. 16. Trend chart of acoustic emission and strain energy of reinforced concrete slab under fatigue load. (**a**) Corrosion rate 0%, (**b**) Corrosion rate 10%, (**c**) Corrosion rate 25%, (**b**) Corrosion rate 40%.

structure elastically, storing energy in the form of strain energy, which increases rapidly at this stage. With continued loading, microcracks begin to form, and both concrete and reinforcement progressively enter the elastic–plastic stage. Uncorroded specimens, due to their stronger internal integrity, can sustain larger loads and store more strain energy, leading to higher peak values. By contrast, corrosion weakens the steel–concrete bond, increases initial structural damage, and promotes microcrack initiation under lower loads. As a result, more energy is consumed in crack generation and propagation, reducing the storable strain energy and lowering its peak. With further cycling, microcracks expand and coalesce into macrocracks, diminishing the structure's load-bearing capacity. Consequently, the stored strain energy begins to be released, manifesting as a decline in strain energy. In specimens with severe corrosion, damage accumulates more rapidly, leading to earlier structural deterioration and a steeper energy drop.

At the microscale, the fatigue behavior of reinforced concrete is governed by particle-level mechanisms, as concrete is composed of discrete aggregates. During early fatigue loading, external forces cause slight adjustments in particle positions, storing elastic potential energy that appears as an increase in strain energy. In uncorroded specimens, particle bond strength (9.2 MPa) and tensile strength (4.5 MPa) are relatively high, allowing significant elastic deformation and energy storage. In contrast, corrosion weakens both the steel–concrete interface and inter-particle bonds. For specimens with corrosion rates of 10%, 25%, and 40%, bond strengths decrease to 7.9, 5.3, and 1.5 MPa, while tensile strengths drop to 3.8, 2.7, and 0.9 MPa, respectively. Under these weakened conditions, sliding and bond breakage between particles occur under lower loads, dissipating energy and reducing the amount of elastic energy that can be stored. During Stage II, relative particle motion and bond breakage reach a quasi-stable state, with limited energy release and low AE activity. This reflects a balance between microcrack growth and structural resistance. In Stage III, however, deterioration accelerates: inter-particle bonds fail rapidly, coarse aggregates fracture, and microcracks expand and interconnect. The stored elastic energy is released in bursts, producing numerous new microcrack surfaces and increased particle displacement. In specimens with higher corrosion rates (25% and 40%), weaker constraints allow easier bond breakage and more violent energy release. As a result, strain energy peaks earlier and declines more steeply. As failure approaches, extensive bond breakage and macrocrack formation occur, releasing large amounts of strain energy and generating a surge in AE events.

In summary, the microscale perspective underscores the crucial link between particle-level bond degradation and the macroscopic fatigue response of corroded reinforced concrete. These findings confirm the value of AE signals and strain energy evolution as reliable indicators for monitoring structural damage progression.

Particle contact force and force-chain network analysis

Force-chain refers to the chain structure formed by interparticle contact forces, and its strength reflects the magnitude of particle interactions. Under cyclic loading, the evolution of internal force-chains and their strength distribution in reinforced concrete slabs can be analyzed in detail using the PFC discrete element method. To clarify the above phenomena, this section presents an in-depth analysis of the force-chain evolution in uncorroded slabs under fatigue loading, as well as the force-chain distribution of specimens with different corrosion rates at complete failure (see Figs. 17 and 18).

Stage I: At the initial stage, particle interactions form the first force-chain network. The chains are relatively evenly distributed, primarily along the load transfer path. The strength distribution shows moderate dispersion, with the maximum force-chain strength only 1.9×10^3 N. This occurs because the initial particle contacts remain relatively stable and no significant stress concentrations have yet developed. Microscopically, the bond between the mortar matrix and coarse aggregates facilitates load transfer. Particles undergo only slight elastic deformation, storing minimal elastic energy, and generating few AE events. At this stage, the skeleton structure remains stable and effectively transmits external loads. As cyclic loading progresses, micro-scale interactions intensify, and local stress concentrations begin to develop, leading the structure into Stage II.

Stage II: Some interparticle bonds begin to fail due to stress concentrations, leading to the reconstruction of force-chains. Certain chains are interrupted while new ones form between neighboring particles to maintain load transfer. Force-chain strength gradually stabilizes and becomes more uniformly distributed. Near microcracks and stress concentration zones, however, large fluctuations appear, and the maximum force-chain strength rises to 3.3×10^4 N. This increase reflects intensified particle fragmentation, rotation, and slip, which shift higher loads onto certain particles and strengthen localized force-chains. Energy accumulation becomes more evident, with part of the stored energy consumed in particle rotation, sliding, and bond breakage. Despite these local fluctuations, the skeleton structure remains largely intact, the overall rate of internal damage grows slowly, and AE events remain low. Eventually, accumulated damage pushes the structure into Stage III.

Stage III: Numerous microcracks expand and coalesce into macrocracks. Force-chains undergo severe disruption: many break apart, and the overall load-transfer path collapses. The strength distribution becomes highly uneven. Around cracks, force-chain strength approaches zero, while in undamaged areas it still decreases sharply, with a maximum strength of only 7.4×10^3 N. At this point, extensive particle breakage occurs, interparticle interlocking fails, and rotation and slip intensify. The bond strength between particles diminishes drastically, the skeleton structure disintegrates, large amounts of energy are suddenly released, and AE events increase sharply. This stored energy is primarily consumed by crack propagation and particle movement, causing the slab's bearing capacity to decline rapidly and ultimately resulting in structural failure.

Figure 18 shows the force-chain distribution of reinforced concrete slabs with different corrosion rates at complete fatigue failure. The evolution of the force-chain network clearly differs across corrosion levels. In the uncorroded specimen (0%), the network maintains a relatively intact skeleton after failure. Strong chains account for about 25% of the network, oriented mainly at 45°. The maximum force-chain strength reaches 7.4×10^3 N, concentrated at aggregate contacts and the steel bar–concrete interface. Weak chains form an isolation zone around the primary crack, with a width of roughly 3–5 times the average particle size. As

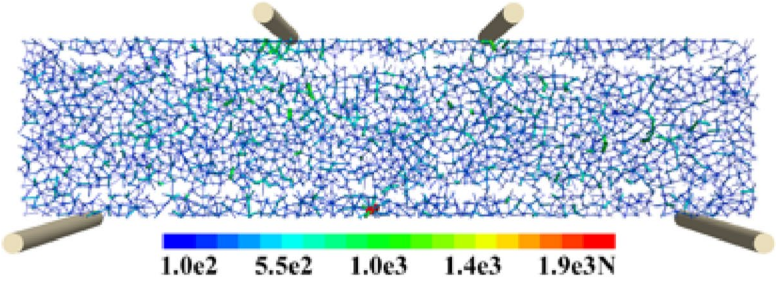

(a) stage I

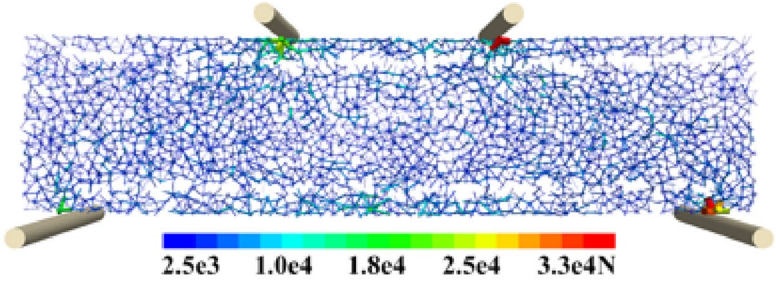

(b) stage II

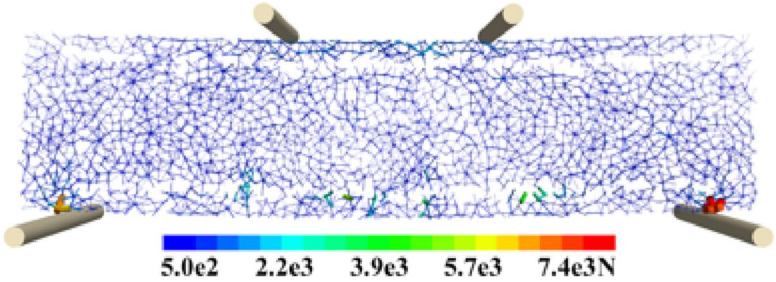

(c) stage III

Fig. 17. Force-chain evolution diagram of uncorroded reinforced concrete slab under fatigue load. (**a**) stage I, (**b**) stage II, (**c**) stage III, (**d**) Comparison of force chain strength with structural stiffness and deflection at different stages.

corrosion progresses, significant changes occur in both network strength distribution and skeleton integrity. At 10% corrosion, anisotropy becomes pronounced: the strong chain proportion falls to 18%, strength fluctuations intensify, and the maximum strength drops to 5.5×10^3 N. Around the reinforcing steel bar, a sparse force-chain zone of 2–3 mm develops, where contact forces attenuate gradually. At 25% corrosion, strong chains shrink to 12%, with maximum strength reduced to 3.8×10^3 N, localized in isolated “force-chain islands” formed by unbroken aggregates. At 40% corrosion, the network essentially collapses: strong chains account for less than 8%, the maximum strength falls to only 6.2×10^2 N, weak chains dominate, bond forces at the steel bar–concrete interface nearly vanish, and the structure completely loses load-bearing capacity.

Overall, differences in the evolution of force-chain networks at varying corrosion rates arise from the coupled evolution of bond energy and skeleton integrity. In uncorroded specimens, strain energy is distributed relatively evenly, with high energy storage at the cement mortar–aggregate interface. This stable distribution preserves skeleton integrity, and the network develops an optimal 45° load transfer path. When local strain energy exceeds the ultimate strength of coarse aggregates, particles fracture[44], producing fines that increase energy fluctuations and trigger particle slip and rotation. However, since the skeleton remains intact, bond performance at the steel bar–concrete interface is strong[45], slip is limited, and efficient load transfer is maintained, supporting high peak force-chain strength. With increasing corrosion, energy distribution and load transfer paths are progressively compromised, driving the transition from ductile to brittle behavior.

At 10% corrosion, strain energy storage becomes spatially differentiated, especially around reinforcement, where bond energy declines and load transfer shifts to aggregate-rich zones. This redistribution weakens the skeleton[46], introduces anisotropy, and reconstructs portions of the load transfer path through aggregate rotation. Meanwhile, corrosion severely degrades steel bar–concrete bond strength, reducing strain energy transmission through bonds. The shear stress once carried by bonds is redirected into aggregate contact and sliding, which increases frictional energy dissipation but lowers maximum force-chain strength.

At 25% corrosion, ITZ degradation reduces strain energy storage efficiency by over 60%. Energy is forced to concentrate within isolated “force-chain islands” formed by intact aggregates[47]. This energy localization

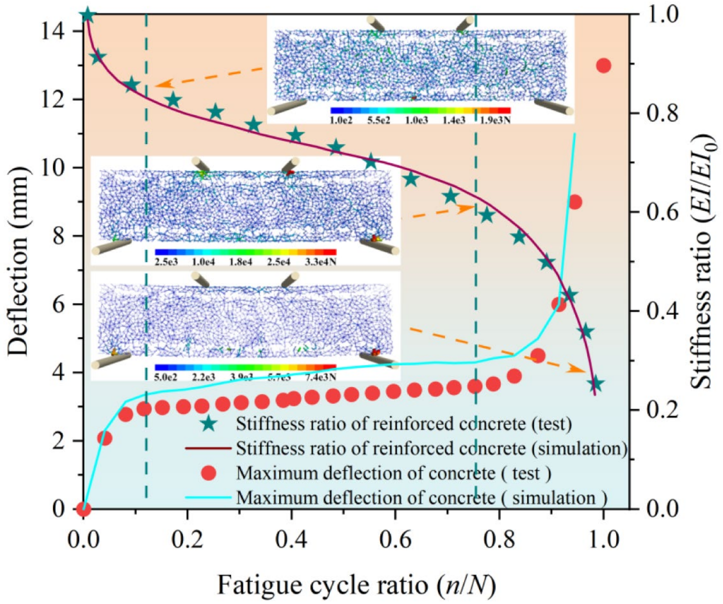

(d) Comparison of force chain strength with structural stiffness and deflection at different stages

Fig. 17. (continued)

underlies the embrittlement failure mode. Particle rotation and slip intensify, widespread bond failure occurs, and the skeleton becomes fragmented. Energy dissipation accelerates, friction and cohesion decline sharply, and only limited load transfer persists within local islands.

At 40% corrosion, multiple coupled mechanisms drive collapse. Bond strain energy storage falls by more than 80%, producing a "short-circuit" effect in energy transfer. The steel bar–concrete interface fails almost completely, and the bond network collapses[47]. Interparticle adhesion is nearly lost, allowing particles to move freely and dissipate energy rapidly. Although aggregates rotate and occasionally reconstruct new force-chains, these processes primarily manifest as network collapse. The proportion of strong chains drops dramatically, the skeleton disintegrates, and frictional and cohesive forces vanish, destroying the transfer path. At this point, the material undergoes a critical phase transition—from a continuous medium to a discrete particle system. Once corrosion exceeds 25%, the primary energy dissipation mechanism shifts from bond fracture to particle friction and slip. This fundamental transformation causes the final collapse of the force-chain network, observed macroscopically as a transition from ductile failure to brittle collapse.

Conclusion

In this study, a 3D particle flow numerical model of reinforced concrete slabs was established using 3D scanning technology, Fish programming, and the discrete element method. Fatigue simulations were conducted on specimens with varying corrosion rates to elucidate the microscopic mechanisms underlying macroscopic structural responses. The main conclusions can be summarized as follows:

(1) Dynamic stiffness and deflection were adopted as indicators to evaluate the fatigue performance of corroded slabs. The fatigue process exhibited three distinct stages. For uncorroded specimens, stiffness degradation was relatively mild, with residual stiffness reaching approximately 60%. As corrosion intensified, stiffness deteriorated more rapidly, residual stiffness decreased, and deflection increased. Corrosion weakened the bond strength at the steel bar–concrete interface, disrupted the skeleton structure, and shifted the load transfer path from global coordination to localized bearing. Consequently, the overall capacity declined, and the failure mode transitioned from ductile to brittle.

(2) The fatigue failure of RC slabs evolved through three stages: crack initiation, stable propagation, and instability. Initially, microcracks appeared in stress concentration zones and extended along the ITZ. These cracks gradually developed into main cracks with relatively slow propagation. In the final stage, cracks expanded rapidly, penetrating the entire section and causing structural failure. Corrosion substantially altered the failure mode: uncorroded slabs exhibited ductile bending failure (*M*-type cracks), whereas higher corrosion rates progressively induced bending–shear mixed failure (*N*-type), brittle shear failure (*Y*-type), sudden splitting (*H*-type), and a shift from distributed to localized damage.

(3) Microcrack evolution and energy dissipation mechanisms. By integrating discrete element modeling with AE analysis, the study clarified the evolution of microcracks and energy dissipation in slabs with different

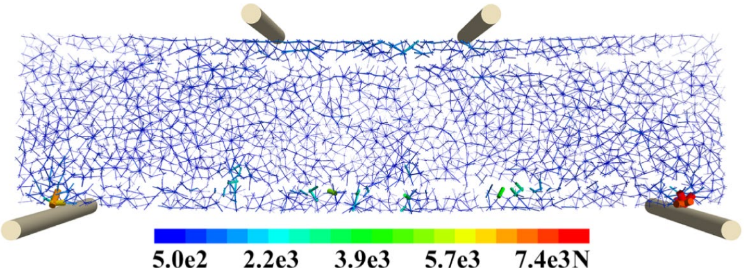

(a) Corrosion rate 0%

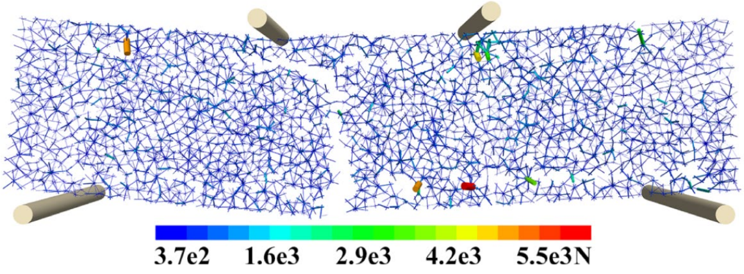

(b) Corrosion rate 10%

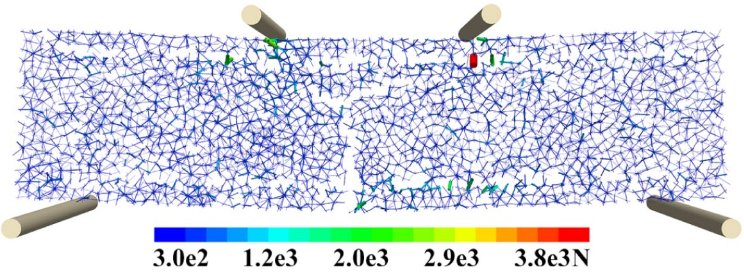

(c) Corrosion rate 25%

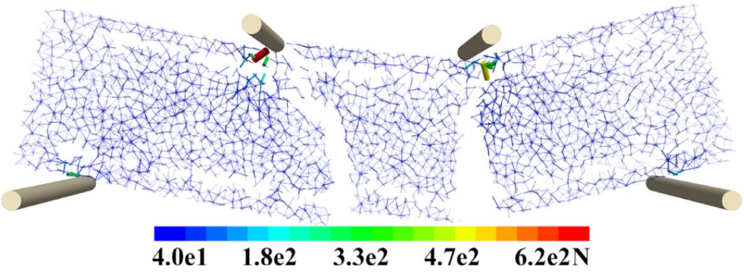

(d) Corrosion rate 40%

Fig. 18. Force-chain distribution of reinforced concrete slabs with different corrosion rates under fatigue load at residual strength. (**a**) Corrosion rate 0%, (**b**) Corrosion rate 10%, (**c**) Corrosion rate 25%, (**d**) Corrosion rate 40%.

corrosion rates. AE activity demonstrated a clear three-stage pattern: microcrack initiation, stable crack development, and rapid crack propagation with structural instability. In Stage I, higher corrosion rates accelerated the increase in AE events and strain energy, although absolute values remained low. In Stage II, AE activity stabilized, but higher corrosion rates corresponded to lower values. In Stage III, AE events and strain energy rose sharply, while peak strain energy decreased with increasing corrosion, showing a more pronounced decline. Macroscopically, corrosion shortened the elastic stage, degraded the steel bar–concrete interface, and intensified internal damage; microscopically, it weakened particle bonding and reduced the material's energy storage capacity.

(4) Evolution of internal force-chain networks. The DEM further revealed the transformation of force-chain networks under the coupled action of cyclic loading and corrosion. For uncorroded specimens, force-chains in Stage I were uniformly distributed, with a maximum strength of 1.9×10^3 N. In Stage II, the force-chains were reconstructed, and maximum strength increased to 3.3×10^4 N. In Stage III, widespread chain fracture

led to uneven distributions, reducing maximum strength to 7.4×10^3 N. Corrosion exerted a pronounced effect on both the distribution and strength of the force-chain network. In uncorroded specimens, force-chains were oriented at approximately 45°, with strong chains accounting for about 25%. At a corrosion rate of 10%, the proportion of strong chains fell to 18% and maximum strength declined to 5.5×10^3 N. For specimens with 25% and 40% corrosion, the strong-chain proportion decreased further to 12% and less than 8%, with maximum strengths of 3.8×10^3 N and 6.2×10^2 N, respectively. This progression illustrates a transition in the force-chain network from ductile failure to brittle collapse.

Limitations

This study employed DEM simulations to investigate fatigue failure mechanisms in RC slabs under combined corrosion and cyclic loading. However, several limitations should be noted.

First, although particle breakage effects were incorporated, the modeling of mechanical interlocking between corroded rebar and surrounding concrete remained idealized. This may have introduced quantitative errors in simulating interfacial slip and damage progression.

Second, the loading conditions examined were restricted to constant-amplitude sinusoidal fatigue. Real-world scenarios often involve variable-amplitude or impact loads, which may produce markedly different damage patterns. Similarly, only four corrosion levels (0%, 10%, 25%, and 40%) were considered, leaving out potential threshold effects (e.g., around 30%) that could trigger abrupt shifts in structural behavior. These constraints limit the generalizability of the findings.

Finally, experimental validation was limited. Due to a lack of data under combined corrosion–fatigue conditions, the simulations were primarily benchmarked against tests performed under either corrosion or fatigue alone. Although calibration ensured macroscopic consistency, microscale validation—such as linking AE signal evolution with crack propagation—remains relatively weak, underscoring the need for targeted experimental investigations.

Future work

Although this study advances understanding of corrosion–fatigue coupling in RC slabs, further research is needed in several areas.

First, the simulation framework should be expanded to account for multi-factor coupling. In addition to constant-amplitude fatigue, future models could integrate environmental influences such as temperature variations, wet–dry cycles, and chloride penetration. Such multi-field coupling would better reflect real service conditions. Extending the analysis to variable-amplitude fatigue loading would also improve the engineering relevance of damage evolution predictions.

Second, experimental validation should be strengthened. Large-scale model tests incorporating AE monitoring, strain measurements, and digital image correlation could be conducted to validate both macroscopic and microscopic aspects of the simulations. At the same time, refinements in DEM parameterization—particularly regarding the ITZ and the dynamic expansion of corrosion products—would improve representation of interfacial degradation.

Finally, predictive modeling of fatigue life presents a promising direction. By leveraging the macro–meso correlations identified in this study, machine learning approaches could be developed to integrate multiple factors, including corrosion rates and loading histories. Such models would enhance the ability to estimate residual service life in existing bridges. Moreover, characteristic AE features identified at different corrosion stages could serve as early-warning indicators, providing a theoretical basis for structural health monitoring and proactive maintenance strategies.

Data availability

The discrete element model datasets generated and analyzed during the current study are available from the corresponding author upon reasonable request (contact: wangshuyong163@163.com). All data supporting the findings of this study are included within the article.

Received: 11 June 2025; Accepted: 3 December 2025

References

1. Fan, L. *Bridge Engineering* (China communications, 2014).
2. Pang, L. *Identification of Fatigue Damage and Prediction of Fatigue Life of Reinforced Concrete slab* (Southeast University, 2004).
3. Wang, Y. et al. Static and fatigue flexural performance of ultra-high performance fiber reinforced concrete slabs. *Eng. Struct.* **231**, 111728 (2021).
4. Liu, R. & Yang, Y. Research on fatigue performance of steel-plate-concrete composite slab. *Thin-Walled Struct.* **160**, 107339 (2021).
5. Mai, G. et al. Fatigue performance of basalt fibre-reinforced polymer bar-reinforced sea sand concrete slabs. *J. Mater. Res. Technol.* **22**, 706–727 (2023).
6. Yan, L. et al. Experimental study on fatigue damage of continuous steel–concrete composite beam by acoustic emission. *Structures* **57**, 105185 (2023).
7. Zou, C. et al. Fatigue performance simulation of reinforced concrete beams externally strengthened with side bonded CFRP sheets. *Eng. Struct.* **316**, 118530 (2024).
8. Al-Rousan, R. Z., Alhassan, M. & Al-wadi, R. Nonlinear finite element analysis of full-scale concrete Bridge deck slabs reinforced with FRP bars. *Structures* **27**, 1820–1831 (2020).
9. Uddin, A. et al. Mechanisms of crack propagation due to corrosion of reinforcement in concrete by AE-SiGMA and BEM. *Constr. Build. Mater.* **18** (3), 181–188 (2004).
10. Ihsan, M. et al. Simulation of corrosion field measurement on reinforced concrete using BEM. *J. Mech. Eng. Sci.* **15** (2), 8072–8081 (2021).

11. Faron, A. & Rombach, G. A. Simulation of crack growth in reinforced concrete beams using extended finite element method. *Eng. Fail. Anal.* **116**, 104698 (2020).
12. El Yassari, S. & El Ghoulbzouri, A. Numerical simulation of fiber-reinforced concrete under Cyclic loading using extended finite element method and concrete damaged plasticity. *Int. J. Eng. Trans. A*. **36** (10), 1815–1826 (2023).
13. Yu, S. et al. Insights into the frost cracking mechanisms of concrete by using the coupled thermo-hydro-mechanical-damage meshless method. *Theor. Appl. Fract. Mech.* **136**, 104814 (2025).
14. Du Longji. *Research on Ultimate Bearing Capacity of Reinforced Concrete Beams Based on PFC* (Chang 'an University, 2018).
15. Luo, C. et al. Analysis of the fatigue mechanism of cement-stabilized macadam mesoscopic intrinsic contact based on the damage accumulation–energy dissipation method. *Iran. J. Sci. Technol. Trans. Civ. Eng.* **47** (4), 2033–2049 (2023).
16. Wang, P. et al. DEM analysis on the role of aggregates on concrete strength. *Comput. Geotech.* **119**, 103290 (2020).
17. Nitka, M. & Tejchman, J. Comparative DEM calculations of fracture process in concrete considering real angular and artificial spherical aggregates. *Eng. Fract. Mech.* **239**, 107309 (2020).
18. Wang, S., Chen, G. & Zhang, L. Parameter inversion and microscopic damage research on discrete element model of cement-stabilized steel slag based on 3D scanning technology. *J. Hazard. Mater.* **424**, 127402 (2022).
19. Huang, P. et al. Concrete failure simulation method based on discrete element method. *Eng. Fail. Anal.* **139**, 106505 (2022).
20. Gong, F. et al. A review on the simulation of aggregate morphologies in mixture performances based on discrete element method. *Constr. Build. Mater.* **385**, 131522 (2023).
21. Liu, M. & Wang, F. Numerical simulation of influence of coarse aggregate crushing on mechanical properties of concrete under uniaxial compression. *Constr. Build. Mater.* **342**, 128081 (2022).
22. Jin Lei, Z. et al. Large triaxial numerical simulation of soil-rock mixture based on irregular particle discrete element method. *J. Geotech. Eng.* **37** (05), 829–838 (2015).
23. Du Xin, Z. et al. Three-dimensional discrete element modeling of irregular shaped particles based on CT scanning. *J. Shanghai Jiaotong Univ.* **45** (5), 711–715 (2011).
24. Wenjie, X. et al. Numerical simulation of meso-structure and mechanical characteristics of soil-rock mixture. *J. Rock. Mech. Eng.* **26** (2), 300–311 (2007).
25. Ding Xiuli, L., Yaoxu, W. & Xin Particle flow simulation of mechanical properties of soil-rock mixture based on digital images. *J. Rock. Mech. Eng.* **29** (3), 477–484 (2010).
26. Zhang Qiang, W. et al. Particle flow simulation study on deformation and failure mechanism of soil-rock mixture under different confining pressure loading methods. *J. Geotech. Eng.* **40** (11), 2051–2060 (2018).
27. Zhang, Q. et al. 3D random reconstruction of meso-structure for soil-rock mixture and numerical simulation of its mechanical characteristics by particle flow code. *Chin. J. Geotech. Eng.* **41** (01), 60–69 (2019).
28. Zhang, Q. et al. Discrete element simulation of large-scale triaxial tests on soil-rock mixtures based on flexible loading of confining pressure. *Chin. J. Geotech. Eng.* **41** (08), 1545–1554 (2019).
29. Zhao, X. et al. Fatigue damage numerical simulation of cement-treated base materials by discrete element method. *Constr. Build. Mater.* **276**, 122142 (2021).
30. Potyondy, D. O. & Cundall, P. A. A bonded-particle model for rock. *Int. J. Rock Mech. Min. Sci.* **41** (8), 1329–1364 (2004).
31. Liu, G. *Discrete Element Modelling of Asphalt Concrete Reinforced with Fiber Glass grids* (Université de Strasbourg, 2019).
32. Le, V. T. et al. A two-surface contact model for DEM and its application to model fatigue crack growth in cemented materials. *Int. J. Plast.* **166**, 103650 (2023).
33. Ali, Y. M. S. et al. *Static and Fatigue Behavior of Concrete Bridge Deck Slabs Reinforced with BFRP and Steel bars//Structures*, vol. 65, 106707 (Elsevier, 2024).
34. Wang, C. *Experimental and Theoretical Analysis of Reinforced Concrete Members Under Corrosion Fatigue Condition* (Dalian University of Technology, 2004).
35. Yuan, H., Weijian, Y. & Chao, H. Corroded reinforced concrete beams under low-speed and low-cycle fatigue loads. *Constr. Build. Mater.* **186**, 644–651 (2018).
36. Xu, J. et al. Fatigue life prediction of fatigue damaged and chloride corroded RC beams. *J. Build. Struct.* **43** (S1), 69–76 (2022).
37. Sadeghi, K. & Nouban, F. Global and local cumulative damage models for reinforced concrete structures subjected to monotonic, cyclic, or fatigue loading. *Int. J. Civ. Eng.* **15** (7), 1063–1075 (2017).
38. Noorsuhada, M. N. An overview on fatigue damage assessment of reinforced concrete structures with the aid of acoustic emission technique. *Constr. Build. Mater.* **112**, 424–439 (2016).
39. Wang, S. Y. *Research on Static and Dynamic Constitutive and Road Explosion Damage Effect of Cement-Stabilized Steel Slag* (Xinjiang Agricultural University, 2023).
40. Wu, C. *Experimental Study of Fractal Dimension of Acoustic Emissions Signal on the Damage Process of Reinforced Concrete beam* (Jiangsu University, 2016).
41. Gu, A. *Acoustic Emission Mechanisms and Characteristics of Damage Detection in Reinforced Concrete Components* (Jiangsu University, 2015).
42. Leng, J. et al. *Feature Extraction of Acoustic Emission Signals for Fatigue Damage of In-service Components*, vol. 48, 186–192 (Chemical Engineering & Machinery, 2021).
43. Fan, X., Hu, S. & Lu, J. Acoustic emission characteristics identification and related parameters influence of reinforced concrete fracture process. *Scientia Sinica (Technologica)*. **45** (08), 849–856 (2015).
44. Wang, X. et al. An elastic and brittle model with damage and application in study on rock localized failures. *J. Basic. Sci. Eng.* **20** (04), 642–653 (2012).
45. Zheng, X. *Research on Dynamic Bond Behavior between Corroded Steel Bar and Concrete* (Hohai University, 2004).
46. Li, Y. *Study on Time-varying Properties of Load Bearing-Corroded Reinforced Concrete Structures* (Yangzhou University, 2018).
47. Qin, C. & Zhang, C. Study of dynamic behavior of concrete under splitting tensile tests based on mesomechanics. *Rock. Soil. Mech.* **31** (12), 3771–3777 (2010).

Acknowledgements

The authors gratefully acknowledge the financial support provided by the 2025 Taizhou Science and Technology Program Project (Grant No. 25nyb10) and Taizhou University Scientific Research Start-up Fund Project (Grant No. T20250101010). At the same time, we would also like to thank Dr. Xiao Fu for her help and assistance with this paper.

Author contributions

Shuyong Wang and Qiu Zhao wrote the main manuscript text and Pengcheng Song and Fei Yang prepared Figs. 1, 2, 3, 4, 5, 6, 7, 8, 9, 10, 11, 12, 13, 14, 15, 16, 17 and 18. All authors reviewed the manuscript.

Funding

This research was supported by 2025 Taizhou Science and Technology Program Project (Grant No. 25nyb10) and Taizhou University Scientific Research Start-up Fund Project (Grant No. T20250101010).

Declarations

Competing interests

The authors declare no competing interests.

Additional information

Correspondence and requests for materials should be addressed to S.W. or Q.Z.

Reprints and permissions information is available at www.nature.com/reprints.

Publisher's note Springer Nature remains neutral with regard to jurisdictional claims in published maps and institutional affiliations.

Open Access This article is licensed under a Creative Commons Attribution-NonCommercial-NoDerivatives 4.0 International License, which permits any non-commercial use, sharing, distribution and reproduction in any medium or format, as long as you give appropriate credit to the original author(s) and the source, provide a link to the Creative Commons licence, and indicate if you modified the licensed material. You do not have permission under this licence to share adapted material derived from this article or parts of it. The images or other third party material in this article are included in the article's Creative Commons licence, unless indicated otherwise in a credit line to the material. If material is not included in the article's Creative Commons licence and your intended use is not permitted by statutory regulation or exceeds the permitted use, you will need to obtain permission directly from the copyright holder. To view a copy of this licence, visit http://creativecommons.org/licenses/by-nc-nd/4.0/.

© The Author(s) 2026